JQS **Journal of Quaternary Science**

QRA
Quaternary Research Association

Palaeoenvironmental reconstruction of Loch Duart (NW Scotland, UK) since the Last Glacial Maximum: implications from a multiproxy approach

JENNIFER TAYLOR,[1]* (iD) DAVID SELBY,[1] JEREMY M. LLOYD,[2] LUCA PODRECCA,[3] ANDREW L. MASTERSON,[3]
BRADLEY B. SAGEMAN[3] and SÖNKE SZIDAT[4] (iD)

[1]Department of Earth Sciences, Durham University, Durham, UK
[2]Department of Geography, Durham University, Durham, UK
[3]Department of Earth and Planetary Sciences, Northwestern University, Evanston, IL, U.S.A.
[4]Department of Chemistry, Biochemistry and Pharmaceutical Sciences & Oeschger Centre for Climate Change Research, University of Bern, Bern, Switzerland

ABSTRACT: A sediment core from the salt marsh fringing Loch Duart, NW Scotland, UK, containing Lateglacial to Holocene sediments, was analysed using a multi-element geochemical approach to elucidate the relative sea level (RSL) and palaeoenvironmental changes associated with the deglaciation of the British and Irish Ice Sheet. Elemental and isotopic measurements of rhenium, osmium, carbon and nitrogen, X-ray fluorescence scanning, radiocarbon dating, and foraminiferal analysis produced a suite of data that complements the existing biostratigraphic framework. This suite of bio-, litho- and chemostratigraphic analyses permits discussion of RSL changes that reflect the interplay between post-glacial eustatic rise and glacio-isostatic adjustment. The osmium-isotope ($^{187}Os/^{188}Os$) data, coupled with a new age–depth model, depict an RSL fall between 16.8 and 14.1 ka cal BP at an average rate of 2 mm a^{-1}. Falling RSL culminates in basin isolation and is followed by subsequent marine inundation from 11.6 ka cal BP. This RSL record preserves the local interaction between glacial isostatic adjustment and glacio-eustatic sea-level change, a relationship that is reflected in the sediment's $^{187}Os/^{188}Os$ signature. This is the first known application of the osmium isotope system in an isolation basin that is shown to be a viable proxy for RSL change, a technique that could be applied to glacially influenced isolation basins globally.
© 2023 The Authors *Journal of Quaternary Science* Published by John Wiley & Sons Ltd.

KEYWORDS: isolation basins; Lateglacial; osmium ($^{187}Os/^{188}Os$); palaeoenvironment; relative sea level

Introduction

The British and Irish Ice Sheet (BIIS) was present over much of the British Isles during the Last Glacial Maximum (LGM). It has long been recognized that the complex relative sea-level (RSL) histories across the British Isles are intimately linked to the history of the BIIS via glacial isostatic readjustment and glacio-eustatic sea-level change (Flemming, 1982; Shennan et al., 2006a, 2006b; Smith et al., 2019). The sedimentary record in Scotland has proven instrumental in refining models of RSL change (Shennan et al., 2000, 2006a; Bradley et al., 2011; Kuchar et al., 2012; Long et al., 2016; Best et al., 2022) which have been heavily influenced by records preserved in isolation basins, a common feature of the NW Scottish landscape. Specifically, isolation basins provide critical sea-level index points that anchor well-constrained sea-level curves for specific areas. One such site at Arisaig has produced a 16 000-year RSL record based on facies modelling and the identification of isolation basins, raised tidal marshes, coastal wetlands and dune systems (Shennan et al., 2005). Similarly, reconstructed RSL histories have been created at Applecross, Kentra and Coigach (Shennan et al., 2000). Recent work has extended the record further north, with two index

points constraining the RSL record during the Lateglacial in the Assynt region (Hamilton et al., 2015). This study aims to expand upon the prior records.

Differentiating periods of marine, brackish and lacustrine deposition in ancient lake settings has traditionally fallen under the purview of biostratigraphic analysis (specifically diatom and foraminiferal studies), as different species of microfauna tolerate different salinities (Lloyd, 2000; Shennan et al., 2000, 2005; Lloyd & Evans, 2002). Unfortunately, this method can be limited by poor microfossil preservation, which necessitates the development of novel palaeoenvironmental methodologies independent of microfossil preservation. C-isotope geochemistry ($\delta^{13}C$) and C/N ratios in bulk organic matter provide one such alternative approach (e.g. Müller and Mathesius, 1999; Andrews et al., 2000). The C-isotope composition of organic matter is offset between marine and terrestrial reservoirs (Arthur et al., 1985) and thus fluctuations in $\delta^{13}C$ of organic carbon can be used to infer fluctuating carbon source. In isolation basins this proxy is especially useful for inferring marine ingression and basin isolation associated with changes in RSL. The close agreement commonly observed between diatom records and $\delta^{13}C$ and C/N records (e.g. Mackie et al., 2005) has bolstered confidence in palaeoenvironmental interpretations using $\delta^{13}C$ and C/N. Further development of these proxies has permitted more intricate inferences on organic carbon fluxes into coastal

*Correspondence: Jennifer Taylor, as above.
E-mail: jtaylor98@hotmail.co.uk

environments ultimately allowing for more meaningful palaeoenvironmental reconstructions (e.g. Lamb et al., 2006).

This study presents promising data on a more novel proxy system – the use of osmium isotope measurements for palaeoenvironmental reconstruction in isolation basins. The osmium isotope ($^{187}Os/^{188}Os$) composition of water-lain organic carbon-bearing sediments records the $^{187}Os/^{188}Os$ of the water column during deposition (e.g. Ravizza & Turekian, 1989; Cohen et al., 1999; Kuroda et al., 2016; Peucker-Ehrenbrink & Ravizza, 2000; Paquay & Ravizza, 2012; Rooney et al., 2016). Notably, the $^{187}Os/^{188}Os$ of seawater is interpreted to reflect an input balance between two main sources: (i) riverine input yielding radiogenic Os sourced from weathered upper continental crust and (ii) mantle-derived Os from submarine volcanism, with input also from cosmic dust and hydrothermal fluids yielding unradiogenic Os (Peucker-Ehrenbrink & Ravizza, 2000). This contrast arises because Os behaves compatibly during melting, whereas Re behaves slightly incompatibly, resulting in low $^{187}Re/^{188}Os$ ratios in the mantle and high $^{187}Re/^{188}Os$ ratios in melts (Walker et al., 1989; Reisberg & Lorand, 1995). The higher $^{187}Re/^{188}Os$ ratios in the crust coupled with the decay of ^{187}Re to ^{187}Os over time produces a wide range of $^{187}Os/^{188}Os$ ratios in crustal materials. This drives the distinctive Os isotopic compositions between mantle and crustal reservoirs. The generally chondritic mantle yields an unradiogenic $^{187}Os/^{188}Os$ ratio with an average of 0.12 whilst continental inputs yield radiogenic $^{187}Os/^{188}Os$ ratios averaging ~1.4 and old crystalline rocks can yield higher ratios of >2 (Peucker-Ehrenbrink & Ravizza, 2000; Peucker-Ehrenbrink and Jahn, 2001). The short residence time of osmium (10^3–10^4 years) in seawater (Peucker-Ehrenbrink & Ravizza, 2000) allows temporally short fluctuations to be identified (e.g. glacial–interglacial cycles) making this system attractive for use as a proxy for palaeoceanographic changes (e.g. Peucker-Ehrenbrink and Ravizza, 2000; Rooney et al., 2016; Ownsworth et al., 2023). Thus, the osmium-isotope composition of seawater and freshwater are typically easily distinguished, with present-day seawater having an $^{187}Os/^{188}Os$ value of ~1.04–1.06 (e.g. Sharma et al., 1997; Levasseur et al., 1998; Burton et al., 1999; Peucker-Ehrenbrink & Ravizza, 2000; Gannoun & Burton, 2014; Rooney et al., 2016) while the osmium-isotope composition of rivers varies considerably; riverine concentrations of Os are strongly dependent on the bedrock composition in the drainage area, with estimates of modern rivers suggesting average $^{187}Os/^{188}Os$ values of ~1.2–1.5 (Levasseur et al., 1999; Peucker-Ehrenbrink & Ravizza, 2000; Peucker-Ehrenbrink, 2002; Lu et al., 2017). Continental $^{187}Os/^{188}Os$ values vary with composition and preferential weathering of more radiogenic sediments (e.g. organic-rich), which can bias the isotopic composition of runoff towards higher (more radiogenic) values (Peucker-Ehrenbrink & Ravizza, 2000). These phenomena make isolation basins an attractive setting for such studies as these basins experience periodic connection to, and isolation from, open seawater and therefore record freshwater and marine intervals that should produce distinctive $^{187}Os/^{188}Os$ signatures.

Our multiproxy study [C/N, $\delta^{13}C_{org}$, $^{187}Os/^{188}Os$, X-ray fluorescence (XRF) and microfossil analysis of foraminifera], utilizing and complementing the framework of the existing microfossil record (Hamilton et al., 2015), aims to reconstruct the palaeoenvironmental and RSL history preserved in Loch Duart, Scotland. Here we demonstrate that the $^{187}Os/^{188}Os$ record is in remarkable agreement with the biostratigraphic reconstructions in an interesting setting that preserves the local interaction between glacial isostatic adjustment and glacio-eustatic sea-level change. This multi-proxy geochemical approach to palaeoenvironmental reconstructions can yield an improved understanding of relative sea-level change, an approach that we suggest could be applied to other study sites bereft of suitable biostratigraphy.
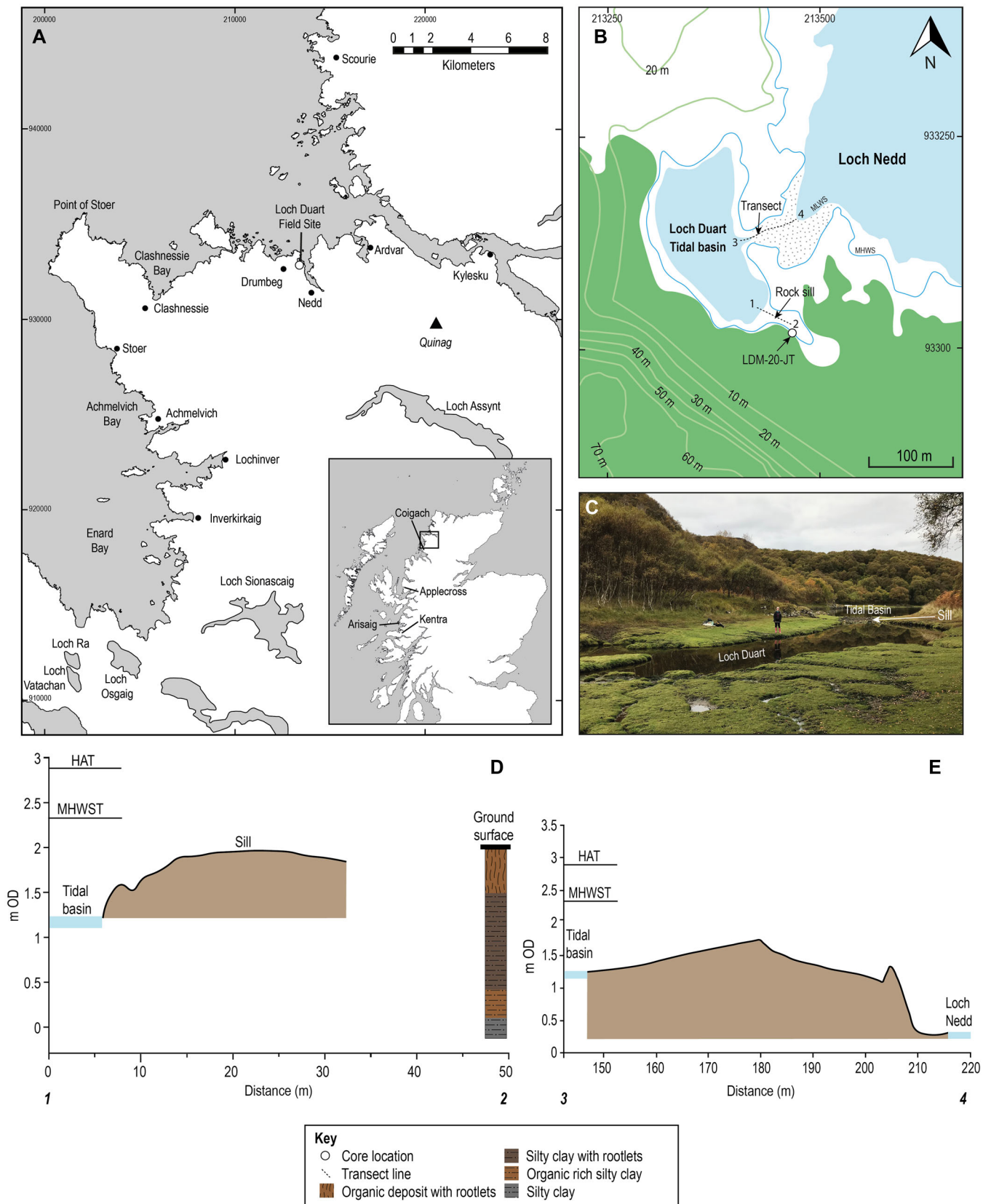
Geographical and geological setting

Loch Duart is located in the Assynt region of north-west Scotland, UK (Fig. 1). The Late Archean Lewisian Gneiss comprises much of the bedrock of this locale, with the north-western edge of the region overlain by Torridonian Group sedimentary rocks (Johnstone & Mykura, 1989). Glacial cycles have reworked the landscape into characteristic 'knock- and-lochan' topography as warm-based glaciers scoured extensive areas producing a setting ideal for lake development (Krabbendam & Bradwell, 2014). Isolation basins record connection to and isolation from the open sea dependent on RSL; basins above highest astronomical tide (HAT) accumulate freshwater sediments whilst lower basins that are inundated during the tidal cycle record brackish to marine sediments (Lloyd, 2000; Lloyd and Evans, 2002). We utilize a new sedimentary core (LDM-20-JT) from a small isolation basin within the fringing salt marsh of the larger Loch Duart tidal basin on Assynt's north coast extracted in 2020, 3 m south-east of the previous study site (LDM-13-1; Hamilton et al., 2015). At the present day, the Loch Duart tidal basin is located on the western shore of Loch Nedd (Fig. 1). The site investigated here is a smaller, largely infilled basin, in the fringing salt marsh of the main tidal basin (referred to hereafter as Loch Duart). The salt marsh itself is ~53 × 23 m and is connected to the Loch Duart tidal basin and therefore Loch Nedd at high tide (Fig. 1b). A bedrock sill is exposed at an altitude of 1.95 m ordnance datum (OD). This sill is partly covered by boulders and separates the main Loch Duart tidal basin from the smaller largely infilled basin (hereafter referred to as LDM) meaning connection only occurs at high tide (Fig. 1d). The bedrock sill is raised 70 cm above the tidal basin which is periodically isolated from Loch Nedd during the tidal cycle (Fig. 1e). There is no riverine input into the basin; rather, input is from solely marine sources. The sedimentary succession at Loch Duart spans from the Lateglacial through the Holocene and records alternating periods of basin isolation and inundation associated with a dynamic RSL history (Hamilton et al., 2015).

Material and methods

Previous work at the study site identified stratigraphic units and the depth of the basin's sill and logged the sediments using the Troels-Smith (1955) descriptive scheme (LDM 13-1; Hamilton et al., 2015). Altitudes and the elevation of the basin's sill were surveyed using a Sokkia Set 6 Total Station and levelled to Ordnance Datum (m OD) using the flush bracket benchmark 12125, located on the south side of Clashnessie Bridge (NC 0557 3080) (Hamilton et al., 2015). This study collected a new Russian core LDM-20-JT (220 cm), adjacent to the previously cored locality, to analyse and test additional proxies against a diatom-based reconstruction (Hamilton et al., 2015). This core comprises six sections 50 cm in length with a diameter of 7.5 cm (0–50, 40–90, 80–130, 120–170, 140–190 and 170–220 cm) that were photographed and described in the field.

X-ray fluorescence and computed tomography analysis

Prior to sampling for geochemical and microfossil analysis, the lowest three core sections (120–170, 140–190 and 170–220 cm) were computed tomography (CT) scanned using the Geotek X-ray

Figure 1. (A) Map of the region surrounding the field site with key locations marked. (B) Map showing the Loch Duart Field site; the location of the core site and survey transects are marked. (C) Field photo of Loch Duart – person for scale standing at the core sample location. (D) Cross-section showing the elevation of the sill and its connection to the adjacent tidal basin along with the sampled core (E) Cross-section of the transect between the tidal basin and Loch Nedd. Adapted from Hamilton et al. (2015). [Color figure can be viewed at wileyonlinelibrary.com]

CT core imaging system (MSCL-XCT) at the Department of Geography of Durham University. This system is used to collect linear digital X-ray images which are then used to produce CT reconstructions and visualize 3D structures within cores. This work identified internal sedimentary structures and helped establish lithofacies boundaries, allowing lithological correlation to the previously studied succession of LDM-13-1 (Hamilton et al., 2015) (Fig. 2).
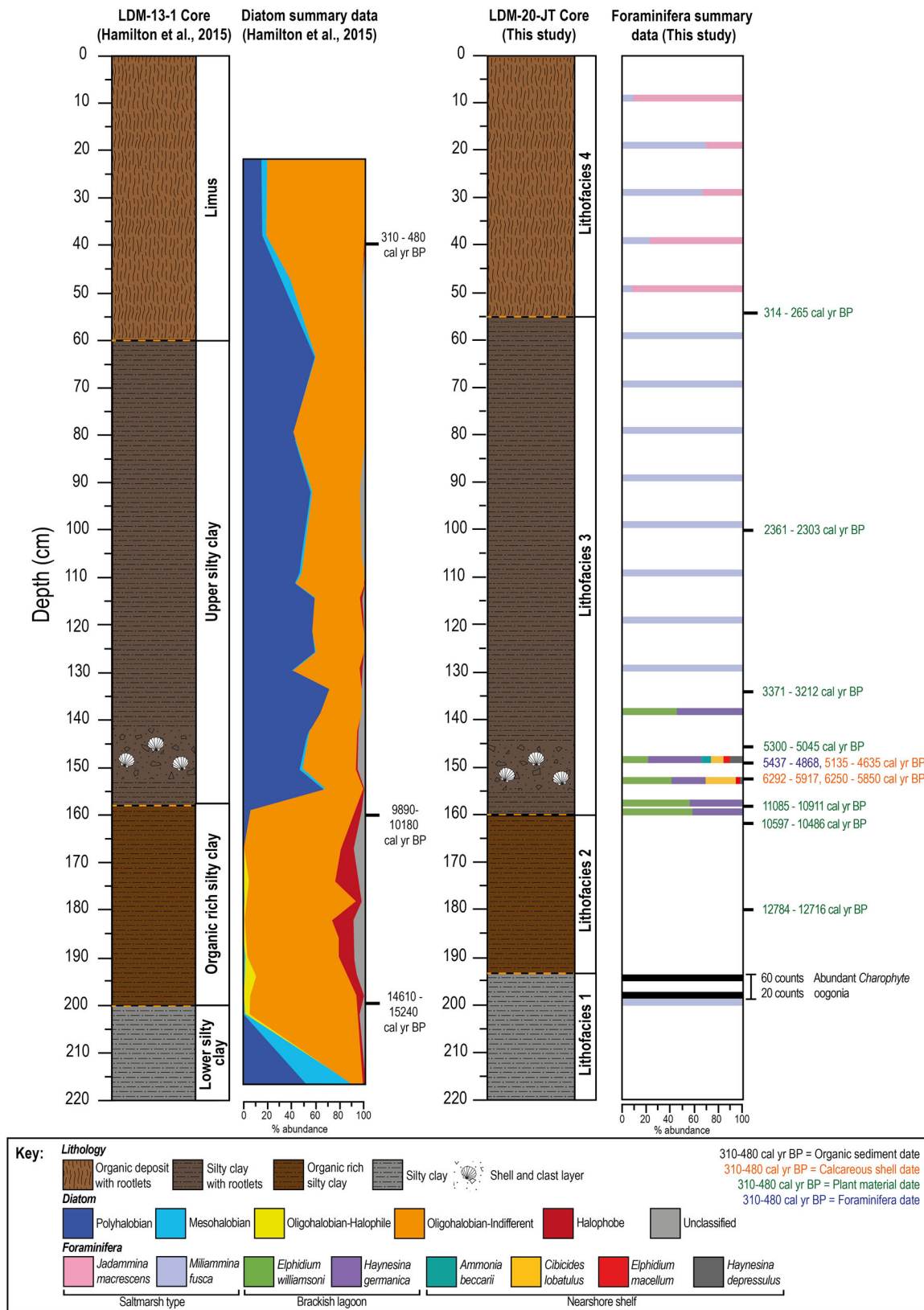
Figure 2. Comparison of LDM-13-1 with a summary of associated diatom analysis adapted from Hamilton et al. (2015) and LDM-20-JT with a summary of associated foraminifera analysis (this study). The radiocarbon dates from both cores are indicated with the colour denoting the type of material dated (black = organic sediment, orange = calcareous shell, blue = foraminifera, green = plant material). [Color figure can be viewed at wileyonlinelibrary.com]

All core sections of LDM-20-JT were scanned using the Geotek X-ray fluorescence (MSCL-XRF) spectrometer in the Geography Department at Durham University (SM 1). This instrument was used to obtain high-resolution (down- and across-core resolutions of 1 and 5 mm, respectively) elemental abundance data from the surface of the sediment cores by bombarding the sample with high-energy X-rays generated in the rhodium X-ray tube. A wide range of elements (Mg to U) can be detected at p.p.m. levels. The detection limits are typically better than 20 p.p.m. for most elements except Al (125 p.p.m.) and Si (190 p.p.m.) used here. As the data are presented in raw counts per second (c.p.s.), values above three

standard deviations are considered valid. To improve the sensitivity of light element measurements (e.g. Mg, Al and Si) a silicon drift detector combined with a helium-flushed measurement cell is used. The data were processed using an MSCL-XYZ Core Workstation.

Rhenium–osmium (Re-Os) analysis

Re-Os analysis was conducted at the Durham Geochemistry Centre (Laboratory for Sulphide and Source Rock Geochronology and Geochemistry and Arthur Holmes Laboratory). Forty samples were taken from Russian core sections (LDM-20-JT), dried at 50 °C, and powdered using an agate pestle and mortar. Powdered samples (0.5-1g) were placed in Carius tubes and spiked with a known quantity of mixed ^{190}Os and ^{185}Re tracer solution along with 8 mL of Cr^{VI}–H_2SO_4 solution that was then heated at 220 °C for 48 hours (Selby & Creaser, 2003). The Os was purified using solvent extraction ($CHCl_3$) with back extraction into HBr, and CrO_3–H_2SO_4–HBr micro-distillation. The Re fraction was purified using NaOH–C_3H_6O solvent extraction and anion chromatography. The Re and Os fractions were loaded onto Ni and Pt filaments, respectively. Isotopic measurements were performed using a ThermoScientific TRITON mass spectrometer via static Faraday collection for Re, and ion-counting was conducted using a secondary electron multiplier in peak-hopping mode for Os. As a result of the young age and low rhenium abundance of the samples measured, the correction for any ingrowth of radiogenic ^{187}Os to the measured present-day $^{187}Os/^{188}Os$ composition is less than that of the minimum $^{187}Os/^{188}Os$ uncertainty (0.004). Therefore, the non-age-corrected, measured present-day $^{187}Os/^{188}Os$ compositions are discussed. The total analytical protocol blanks are 11 ± 2 pg for Re and 0.10 ± 0.02 pg for Os, with a $^{187}Os/^{188}Os$ of 0.21 ± 0.03 (1 SD, $N = 4$). A synopsis of the Re-Os data is presented in Table 1.

To monitor the long-term reproducibility of the Re-Os isotope composition determinations, Re and Os solution standards are routinely analysed. At the time of analysis completion (June 2021), the Durham Romil Osmium Standard (DROsS – 50 pg solution) yielded a running average of 0.16082 ± 0.00061 (1 SD, $N = 830$) for $^{187}Os/^{188}Os$ values, and the rhenium standard solution (Restd – 125 pg solution) yielded a running average of 0.59861 ± 0.0015 (1 SD; $N = 727$) for $^{185}Re/^{187}Re$ values.

Total organic carbon (TOC), $\delta^{13}C_{org}$ and N analyses

Regularly spaced (~10 cm) core sediment samples ($N = 26$) were analysed for weight percent (wt%) TOC, $\delta^{13}C_{org}$ and total nitrogen (TN). An aliquot of sample powder prepared for Re-Os analysis was acidified with 10% HCl to remove any carbonate. All three datasets were collected using a Costech 4010 Elemental Analyser coupled to a Thermo Delta V+ mass spectrometer via a Conflo IV interface at the Northwestern Stable Isotope Biogeochemistry Laboratory (NUSIBL). Samples were combusted over a column of Cr_2O_3 held at 980°C and a Cu reduction column held at 705°C. Elemental information was estimated via cross-calibration with acetanilide organic standards, and isotopic data $\delta^{13}C_{org}$ was determined via the repeated analyses of Indiana University acetanilide ($\delta^{13}C = -29.52‰$) and urea standards ($\delta^{13}C = -8.01‰$) (Schimmelmann et al., 2009). Carbon isotopes are reported with respect to Vienna Pee Dee Belemnite (VPDB). Uncertainty estimates from three duplicates in each run are 0.2% for wt% TOC, 0.03% for TN and 0.24‰ for $\delta^{13}C_{org}$; see Table 1 for data synopsis.

Foraminifera analysis

Foraminiferal assemblages were identified from 1-cm-thick samples taken every 2–10 cm through LDM-20-JT. These samples were washed through 500- and 63-μm sieves and foraminifera were wet-picked and counted from the 63–500-μm size fraction. The taxonomy for foraminifera follows that of Murray (1971, 1979).

Radiocarbon dating

Eleven radiocarbon dates were obtained from core LDM-20-JT and combined with one existing radiocarbon date from core LDM-13-1 (Hamilton et al., 2015) (Table 2). Ten accelerator mass spectrometry (AMS) radiocarbon dating measurements were conducted by Beta Analytic (Miami, FL, USA). One radiocarbon measurement on a mixed sample of benthic foraminifera was conducted at the Laboratory for the Analysis of Radiocarbon, Berne, using MIni CArbon DAting System (MICADAS) AMS (Szidat et al., 2014). The raw ^{14}C ages were calibrated using OxCal 4.4 (Bronk Ramsey, 2009) using the Marine20 and IntCal20 radiocarbon calibration curves (Heaton et al., 2020; Reimer et al., 2020). Recalculated local reservoir corrections (ΔR) are required to account for the 150 ^{14}C years offset between the Marine20 and Marine13 (Heaton et al., 2020; Reimer et al., 2013). A ΔR of -126 ± 58 years (previously 24 ± 58 years using Marine13) (Harkness 1983) was deemed appropriate considering the proximity to core location. This ΔR is comparable with the averaged ΔR from the five nearest data points (Harkness 1983; Cappelli & Austin 2020) in the CALIB marine reservoir correction database (Reimer and Reimer, 2001). Therefore, a local ΔR of -126 ± 58 was used when calibrating with the Marine20 curve. All dates are expressed as calendar years before CE 1950 (cal a BP) and the 1-sigma age ranges are reported in Table 2. The age–depth model for the LDM-20-JT core was created using BACON age–depth modelling software in R (Blaauw & Christen, 2011) from the raw ^{14}C ages (SM 2).

Results

We identify four distinct lithofacies in LDM-20-JT (220 cm). Lithofacies 1 (L1) (220–193 cm) is a pale grey silty clay that is overlain by Lithofacies 2 (L2) (193–160 cm), a dark brown, organic-rich silty clay with abundant rootlets. This is overlain by Lithofacies 3 (L3) (160–55 cm), a dark grey silty clay with a conspicuous layer of clasts and fragmented shells (155–145 cm) up to 3 cm in diameter. Lithofacies 3 is overlain by the uppermost Lithofacies 4 (L4) (55–0 cm), a fine-grained organic deposit with abundant rootlets, silt and clay material.

Lithofacies 1 (L1)

Lithofacies 1 (220–193 cm), is a pale grey silty clay that coarsens slightly upward. We directly correlate L1 with the lower silty clay unit of Hamilton et al. (2015) based on clear lithological contacts, the close (3 m) proximity of the two cores and the increase in Charophyte oogonia and oligohalobian-indifferent genera at the upper transition of LDM-20-JT and LDM-13-1, respectively, which are both markers of a transition in depositional environment (Fig. 2). A radiocarbon bulk sediment age of 14 610–15 240 cal a BP at the upper transition of the lower silty clay unit of core LDM-13-1 (Fig. 2) suggests that this facies transition occurred during the Lateglacial (Hamilton et al., 2015). This age is inferred for the upper transition of L1 in core LDM-20-JT based on lithological correlation with LDM-13-1. Most of L1 lacks abundant

Table 1. Synopsis of wt% C, $\delta^{13}C_{org}$ VPDB, wt% N, C/N, Re and Os isotopic data, Loch Duart, Assynt, Scotland.

Depth (cm)	Wt% C	Wt% C duplicate	$\delta^{13}C_{org}$ VPDB (‰)	$\delta^{13}C_{org}$ VPDB duplicate	Wt% N	Wt% N duplicate	C/N	C/N duplicate	Re (p.p.b.)	±*	Os_T (p.p.t.)	±*	^{192}Os (p.p.t.)	±*	$^{187}Re/^{188}Os$	±*	$^{187}Os/^{188}Os$	±*	rho	% Re blank	% ^{187}Os blank	% ^{188}Os blank
10–11	23.56		−25.65		2.18		10.82		2.37	0.01	63.0	0.4	23.1	0.2	204.0	2.1	1.095	0.011	0.845	2.56	0.16	0.87
20–21	24.9		−25.78		2.20		11.33		8.84	0.01	53.5	0.4	19.6	0.2	895.7	9.3	1.087	0.012	0.939	0.55	0.18	0.99
30–31	23.76		−25.96		1.94		12.24		12.36	0.01	52.1	0.3	19.5	0.2	1263.4	13.2	0.938	0.010	0.934	0.39	0.21	1.00
39–40									10.46	0.01	56.9	0.2	21.1	0.1	985.0	4.8	0.983	0.006	0.808	0.32	0.08	0.38
40–41	24.01		−26.26		1.69		14.21															
50–51	26.24		−26.59		1.78		14.75															
55–56									18.30	0.01	46.2	0.4	17.1	0.3	2129.5	31.1	1.011	0.023	0.638	0.34	0.12	0.59
60–61	16.34		−24.49		1.42		11.54															
70–71	9.77		−20.62		1		9.78															
74–75									24.09	0.01	88.9	0.7	33.3	0.4	1440.4	16.7	0.921	0.018	0.608	0.14	0.05	0.24
80–81	8.29		−20.72		0.84		9.92															
90–91	8.53		−20.83		0.88		9.67		26.78	0.02	79.0	0.4	29.0	0.2	1840.1	10.1	1.093	0.007	0.861	0.15	0.08	0.46
100–101	9.01		−21.59		0.9		9.97															
104–105									18.91	0.01	88.5	0.3	33.2	0.1	1134.3	3.5	0.908	0.004	0.776	0.18	0.05	0.24
110–111	6.33	6.58	−21.00	−20.92	0.63	0.66	10.10	10.04														
120–121	7.95		−21.49		0.7		11.38		18.82	0.06	87.2	0.4	32.3	0.2	1158.8	6.8	0.998	0.006	0.724	0.22	0.08	0.42
129.5–131	7.61		−21.39		0.67		11.40															
130–131									18.71	0.02	80.0	0.3	30.1	0.2	1237.0	6.6	0.876	0.005	0.849	0.18	0.10	0.45
140–141	7.35		−19.68		0.62		11.93		18.97	0.01	84.2	0.3	31.8	0.2	1185.8	5.7	0.832	0.005	0.722	0.16	0.08	0.32
142–144									21.31	0.01	78.8	0.3	29.2	0.1	1452.6	5.0	1.013	0.004	0.817	0.16	0.05	0.28
150.5–151.5	7.54		−20.11		0.57		13.12		14.83	0.01	108.8	0.5	40.0	0.2	736.9	3.5	1.061	0.007	0.693	0.21	0.05	0.25
152–153	7.03		−19.90		0.58		12.12		17.21	0.04	102.4	0.4	38.5	0.2	890.2	4.0	0.887	0.005	0.667	0.18	0.06	0.26
152–153									16.33	0.05	108.8	0.5	41.0	0.2	793.3	5.1	0.871	0.007	0.664	0.25	0.07	0.32
154–155									14.63	0.04	85.8	0.4	31.5	0.2	924.3	6.2	1.091	0.009	0.714	0.28	0.08	0.42
160–161	12.75		−22.07		0.70		18.24		12.58	0.04	256.0	1.0	91.4	0.3	273.9	1.2	1.326	0.006	0.540	0.32	0.02	0.15
165–166	8.87		−19.68		0.52		17.22		15.20	0.01	251.8	1.2	82.9	0.3	364.5	1.3	2.067	0.011	0.702	0.27	0.02	0.16
168–169									11.49	0.04	142.9	1.0	43.3	0.3	528.5	3.5	2.914	0.023	0.643	0.36	0.02	0.31
169–170									20.08	0.01	230.4	1.0	69.5	0.2	575.0	1.4	2.960	0.010	0.691	0.17	0.01	0.12
169–170									16.49	0.01	197.8	1.0	56.1	0.2	584.3	1.9	3.614	0.016	0.711	0.21	0.01	0.14
170–171	10.07		−17.52		0.54		18.59		17.09	0.05	171.0	1.3	46.8	0.3	726.2	4.6	4.020	0.031	0.662	0.24	0.02	0.29
175–176	7.43		−16.84		0.48		15.36		8.79	0.01	153.5	1.0	42.7	0.2	409.7	1.8	3.846	0.023	0.717	0.34	0.02	0.23
178–179									6.43	0.03	192.3	1.9	51.4	0.4	248.9	2.4	4.292	0.053	0.582	0.63	0.02	0.25
180–181	10.62	10.77	−16.70	−17.37	0.68	0.68	15.70	15.84	10.80	0.01	274.2	1.8	69.8	0.3	307.7	1.3	4.887	0.028	0.704	0.39	0.01	0.19
182–183									16.06	0.01	226.7	1.2	60.4	0.2	529.2	1.6	4.346	0.018	0.698	0.21	0.01	0.13
185–186	11.23		−16.75		0.73		15.49		8.82	0.01	302.0	1.6	84.9	0.3	206.6	0.7	3.715	0.016	0.709	0.47	0.01	0.16
190.5–191.5									9.69	0.01	328.5	2.0	99.0	0.4	194.6	0.9	2.958	0.020	0.669	0.35	0.01	0.08
191–192	2.9		−18.53		0.26		11.16		3.97	0.01	131.8	0.7	40.6	0.2	194.3	0.9	2.732	0.014	0.779	1.43	0.02	0.33
195–196									3.22	0.00	100.3	0.7	32.0	0.2	200.4	1.3	2.379	0.023	0.661	0.77	0.02	0.25
197–198									9.88	0.01	455.1	2.3	149.1	0.6	131.8	0.5	2.120	0.012	0.676	0.57	0.00	0.04
200–201	1.04		−19.53		0.09		12.13		3.57	0.01	72.4	0.4	23.9	0.2	296.5	1.9	2.032	0.014	0.881	1.59	0.06	0.56
202–203									2.41	0.00	103.8	0.6	35.8	0.2	134.1	0.7	1.652	0.012	0.683	0.71	0.01	0.11
202–203									2.68	0.00	117.4	0.5	39.6	0.1	134.6	0.5	1.848	0.009	0.659	1.27	0.01	0.10
204–205									3.38	0.00	91.5	0.4	31.9	0.1	210.7	0.9	1.537	0.008	0.736	0.74	0.03	0.25

(Continued)

Table 1. *(Continued)*

Depth (cm)	Wt% C	Wt% C duplicate	$\delta^{13}C_{org}$ VPDB (‰)	$\delta^{13}C_{org}$ VPDB duplicate	Wt% N	Wt% N duplicate	C/N	C/N duplicate	Re (p.p.b.)	±*	Os_T (p.p.t.)	±*	^{192}Os (p.p.t.)	±*	$^{187}Re/^{188}Os$	±*	$^{187}Os/^{188}Os$	±*	rho	% Re blank	% ^{187}Os blank	% ^{188}Os blank
208–209	1.13		−19.73		0.09		12.20		3.12	0.00	90.8	0.4	32.1	0.1	193.0	0.7	1.407	0.006	0.753	1.09	0.04	0.25
209–211									3.62	0.00	100.9	0.7	35.8	0.3	201.2	1.6	1.391	0.016	0.707	0.47	0.02	0.11
211.5–212.5									3.22	0.00	106.3	0.4	38.3	0.1	167.0	0.7	1.238	0.007	0.664	1.06	0.03	0.21
214–215									2.24	0.01	86.8	0.7	31.5	0.3	141.6	1.6	1.175	0.023	0.545	1.51	0.04	0.26
218–220	0.9	0.86	−14.96	−14.70	0.07	0.07	12.42	12.19	1.34	0.00	102.7	0.4	37.8	0.1	70.7	0.3	1.059	0.004	0.575	2.53	0.04	0.21

*All uncertainties are 2σ absolute.

foraminifera with only a small number of *Miliammina fusca* specimens identified at 199 cm, but there are abundant *Charophyte* oogonia present at the upper transition from L1 to L2 (Fig. 3). Both TOC (0.9–1.04 wt%) and nitrogen (0.07–0.09 wt%) concentrations are relatively low and constant throughout L1 (Fig. 3). Similarly, the C/N ratios show little variation upsection (12.13–12.42) (Fig. 3). The carbon isotope record in this basal facies is relatively enriched in the heavy ^{13}C isotope ($\delta^{13}C_{org}$ = −19.73 to −14.96‰). This C-isotope range falls in between the established values of marine particulate organic carbon (POC) and marine dissolved organic carbon (DOC), illustrated by the C/N versus $\delta^{13}C$ biplot (Fig. 4) (Lamb et al., 2006). The XRF elemental analysis reports homogenous Cu-counts across this lithofacies; Se remains similarly consistent through the lower 25 cm of this lithofacies, but it increases prior to the transition into L2 (Fig. 5; S1). The highest Al, Si, K, Ti and Fe counts are recorded in the bottom section of L1, with peaks present between 210 and 215 cm before a gradual decrease upsection. The $^{187}Os/^{188}Os$ values in L1 increase steadily from the base (1.06) to its upper transition (2.38) (Fig. 3). The Re content is relatively stable (1.34–3.62 p.p.b.), with one notable exception at 197–198 cm (9.88 p.p.b.). The $^{187}Re/^{188}Os$ values range from 70.7 to 296.5 and total osmium abundance ranges between 72.4 and 117.4, with a peak at 197–198 cm (455.1 p.p.t.).

Lithofacies 2 (L2)

Lithofacies 2 (193–160 cm) is a dark brown, organic-rich silty clay with abundant rootlets. A radiocarbon date from plant material taken at 180 cm provides an age of 12 784–12 716 cal a BP constraining the lower section of L2 as Lateglacial in age (Figs 2 and 6). Another plant material-based radiocarbon date at 162 cm of 10 702–10 551 cal a BP constrains the upper transition of this lithofacies to the Early Holocene (Figs 2 and 6). Foraminifera are notably absent throughout this lithofacies (Fig. 3). Variable TOC (2.90–12.75 wt%) and N (0.26–0.73 wt%) are observed through L2, and both are relatively elevated compared to L1. Two peaks are recorded at 160.5 cm (12.75 wt% TOC and 0.70 wt% N) and 185.5 cm (11.23 wt% TOC and 0.73 wt% N). The C/N ratios across L2 range between 11.16 and 18.59, displaying a broad peak in the upper 10 cm of the lithofacies (17.22–18.59) (Fig. 3). A broad peak in $\delta^{13}C_{org}$ is also observed through L2; the heaviest $\delta^{13}C$ values reach −16.70‰, with subsequent values decreasing to −22.07‰ at the upper transition. The biplot of C/N versus $\delta^{13}C$ shows L2 samples clustering in the transitional space between the marine DOC and C4 terrestrial plant fields (Fig. 4). This lithofacies is also characterized by notable peaks in Cu and Se counts between 190 and 165 cm juxtaposed against decreases in Al, Si, K, Ti and Fe (Fig. 5; S1). A significant increase in $^{187}Os/^{188}Os$ values is observed across this lithofacies, with an increase from 2.73 at the base of the lithofacies to a broad peak that captures the core's most radiogenic values. This maximum peak in radiogenic $^{187}Os/^{188}Os$ values is observed at 180.5 cm (4.89) with a second smaller peak recorded at 170.5 cm (4.02). Upsection, the $^{187}Os/^{188}Os$ ratio decreases to a value of 1.33 at the upper boundary of the lithofacies (Fig. 3). There are multiple shifts in Re content throughout L2 (3.97–20.08 p.p.b.), with two prominent peaks that closely align with the $^{187}Os/^{188}Os$ record (182.5 cm = 16.06 p.p.b.; 169.5 cm = 20.08 p.p.b.).There are also two peaks in the $^{187}Re/^{188}Os$ record (182.5 cm = 529.2; 170.5 cm = 726.2). Total osmium oscillates with a similar pattern with abundances between 131.8 and 328.5 p.p.t., but shows greater abundances at the base (328.5 p.p.t.) and top (256.0 p.p.t.) of L2, respectively.

Table 2. Synopsis of radiocarbon ages from core LDM-20-JT, Loch Duart, Assynt, Scotland.

Sediment core	Laboratory code	^{14}C age $\pm 1\sigma$ (^{14}C a BP)	Calibrated age (cal a BP)	Depth in core (cm)	Sample type	Reference
LDM-20-JT	Beta - 601750	230 ± 30	314–265	54	Plant material	This study
LDM-20-JT	Beta - 601751	2310 ± 30	2361–2303	100	Plant material	This study
LDM-20-JT	Beta - 601752	3080 ± 30	3371–3212	134	Plant material	This study
LDM-20-JT	Beta - 601753	4500 ± 30	5300–5045	146	Plant material	This study
LDM-20-JT	BE-16154.1.1	4907 ± 81	5437–4868	153.5	Foraminifera sample	This study
LDM-20-JT	Beta - 579376	4680 ± 30	5135–4635	153.5	Calcareous shell fragment	This study
LDM-20-JT	Beta - 579374	5770 ± 30	6292–5917	154	Calcareous shell fragment	This study
LDM-20-JT	Beta - 579375	5690 ± 30	6250–5850	154.5	Calcareous shell fragment	This study
LDM-20-JT	Beta - 590335	9560 ± 30	11085–10911	158	Plant material	This study
LDM-20-JT	Beta - 590336	9390 ± 30	10702–10551	162	Plant material	This study
LDM-20-JT	Beta - 601754	10800 ± 40	12784–12716	180	Plant material	This study
LDM-13-1	Beta - 390107	12670 ± 40	14610–15240	199	Organic sediment	Hamilton et al. (2015)
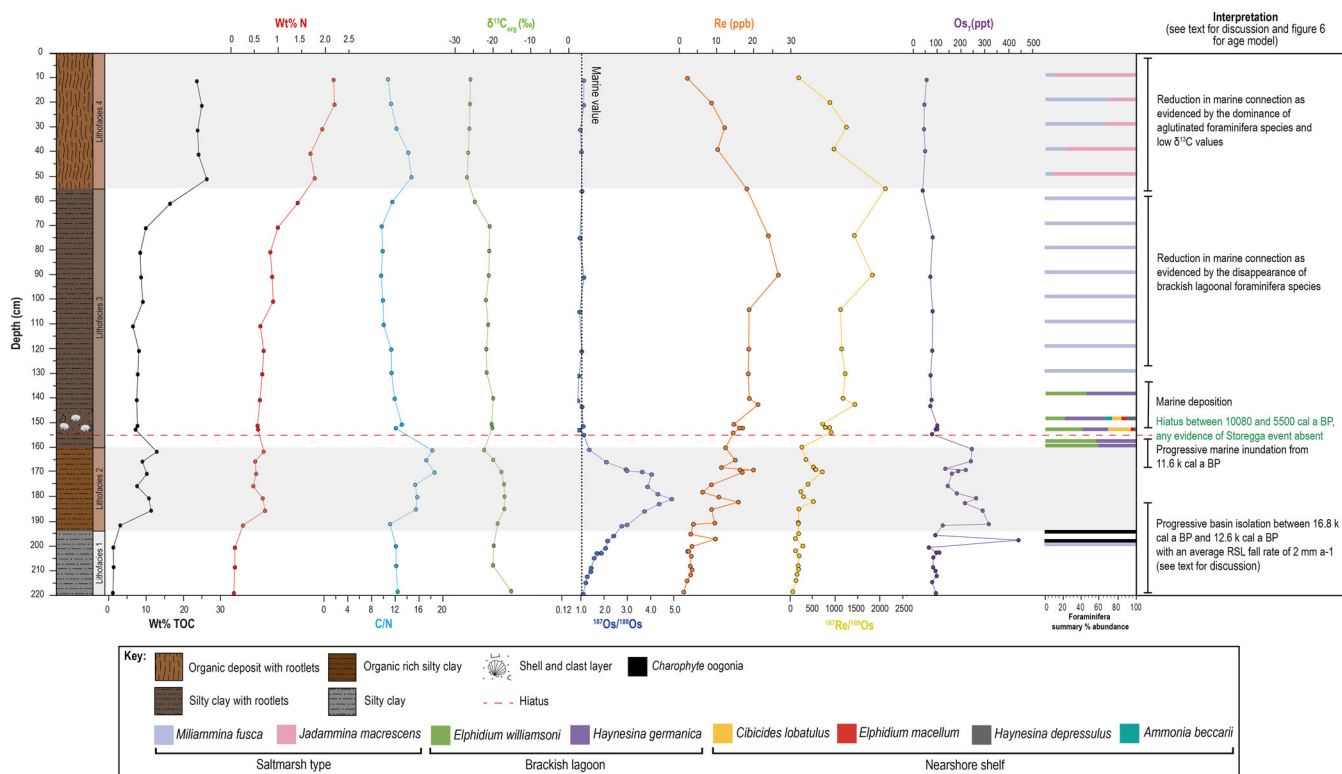
Figure 3. Proxy comparison for LDM-20-JT, including wt% TOC, wt% N, C/N, $\delta^{13}C_{org}$ (‰), $^{187}Os/^{188}Os$, Re (p.p.b.), $^{187}Re/^{188}Os$, Os^T (total p.p.t.) and foraminifera species data. [Color figure can be viewed at wileyonlinelibrary.com]

Lithofacies 3 (L3)

Lithofacies 3 (160–55 cm) is a dark grey fine-grained silty clay notable for a layer of clasts and fragmented shells up to 3 cm in diameter between 145 and 155 cm. A plant material radiocarbon date from the lower boundary (11 085–10 911 cal a BP) indicates deposition during the Early Holocene. Additionally, upsection radiocarbon dates from calcareous shell and plant material record Middle to Late Holocene ages (Table 2, Fig. 6). Foraminiferal diversity reaches a maximum in L3. *Elphidium williamsoni* and *Haynesina germanica* dominate the assemblage between 160 and 140 cm with *Cibicides lobatulus*, *Elphidium macellum*, *Ammonia beccarii* and *Haynesina depressulus* appearing between 153.5 and 140 cm (Fig. 3).

All calcareous species disappear at 130 cm and the agglutinated species, *Miliammina fusca*, defines the micro-fossil record (Fig. 3). The TOC and N contents decrease across the L2–L3 boundary, but both subsequently increase again upsection in L3 (TOC increases from 7.03 to 16.34 wt% and N increases from 0.58 to 1.42 wt% between 152.5 and 60.5 cm). The L3 facies records lower C/N ratios (9.67–13.12) and $\delta^{13}C_{org}$ values (−24.49 to −19.68‰) than L2, forming a well-defined cluster in C/N versus $\delta^{13}C$ space mostly within the marine DOC range, but with some slightly higher $\delta^{13}C$ values within the marine POC range (Fig. 4). The XRF elemental counts show a slight increase in Al, Si, K, Ti and Fe across L3 before ultimately decreasing at the upper transition (Fig. 5; S1).
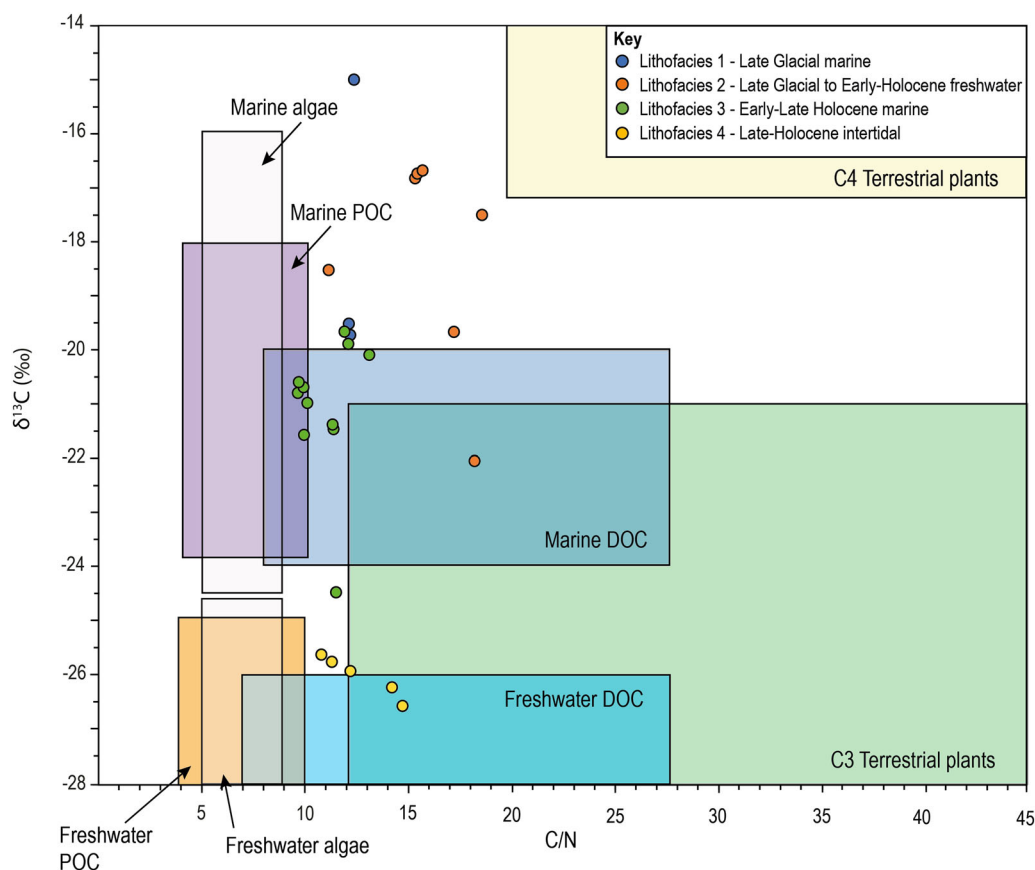
Figure 4. C/N and $\delta^{13}C_{org}$ from bulk organic material from the LDM-20-JT core. The typical $\delta^{13}C_{org}$ and C/N ranges for organic inputs to coastal environments fields are based on Lamb et al. (2006). [Color figure can be viewed at wileyonlinelibrary.com]

The Re and Os elemental abundances of this lithofacies range between 14.63 and 26.78 p.p.b., and 46.2 and 108.8 p.p.t., respectively. Little variation in $^{187}Os/^{188}Os$ (0.83–1.09) with a broadly flat profile is observed in L3, which is distinctly less radiogenic than L2 (Fig. 3). The $^{187}Re/^{188}Os$ values broadly increase upsection, ranging from 736.9 to 2129.5.

Lithofacies 4 (L4)

This uppermost lithofacies (55 cm to core top) is a fine-grained organic-rich silty clay with abundant rootlets. A radiocarbon date at the lower boundary provides an age of 314–265 cal a BP (plant material) (Table 2). Agglutinated foraminifera species (*Jadammina macrescens* and *Miliammina fusca*) dominate this lithofacies with *Jadammina macrescens* appearing just after the transition into L4 and dominating the assemblage, except between 29.5 and 19.5 cm, where *M. fusca* is again more abundant (Fig. 2). TOC varies between 23.56 and 26.24 wt% which is significantly higher than anywhere else in the record (Fig. 3). N content is also greater in L4 than anywhere else in the core; increasing from 1.78 to 2.18 wt%, between 50.5 cm and the surface (Fig. 3). L4 is characterized by isotopically light $\delta^{13}C_{org}$ values (between −26.59 and −25.65‰) and a peak in C/N ratios (14.2–14.7) between 40.5 and 50.5 cm. These peaks are followed by a gradual decrease to lower values upsection, shifting $\delta^{13}C$ versus C/N values into and just above the freshwater DOC field (Fig. 4). There is no apparent trend in Cu, Al, Si, K, Ti, Fe and Se XRF counts between 55 cm and the surface of the core, but these elemental values are systematically lower than in L3 (Fig. 5; S1). The elemental abundance of osmium varies little over this section with values of 52.1–63.0 p.p.t. Both rhenium and $^{187}Re/^{188}Os$ values decrease across the transition between L3 and L4 from 18.30 to 2.37 p.p.b. and

from 2129.5 to 204.0 respectively. The $^{187}Os/^{188}Os$ compositions remain similar to those in L3 and are relatively constant throughout L4 ranging from 0.94 to 1.09.

Chronology

Radiocarbon dates from this study (*N* = 11) were combined with the data from Hamilton et al. (2015) (*N* = 1 at 199 cm) to create an age–depth model using rbacon (Fig. 6; S2). The model suggests that the base of the core represents deposition *c.* 16.8 ka cal BP and that, if constant, sedimentation rate was ~0.1 mm a^{-1} throughout L1. The transition between L1 and L2 dates to 14.1 ka cal BP with sedimentation remaining fairly constant at 0.1 mm a^{-1} through L2. The transition between L2 and L3 is well constrained at 10.6 ka cal BP based on dates above and below the transition. However, the radiocarbon dates (and the age model developed here) suggest a significant hiatus within L3 (Fig. 6) with sedimentation rates varying through L3. A series of radiocarbon dates support the inferred hiatus based on the sharp contact of the shell and clast layer near the base of L3. At 158 cm, a plant material radiocarbon date yields an age of 11 085–10 911 cal a BP whilst just 3.5 cm stratigraphically higher in the core a calcareous shell fragment yields an age of 6250–5850 cal a BP. This shell age is in close agreement with two other calcareous shell fragments collected at 154 cm (6292–5917 cal a BP) and 153.5 cm (5135–4635 cal a BP); it further agrees with a foraminifera radiocarbon date at 153.5 cm (5437–4868 cal a BP). This dramatic difference in radiocarbon dates (~5000 years) over such a short stratigraphic interval (5 cm or less) presents strong evidence of a hiatus. This inferred erosive event occurs within L3 rather than at its base, suggesting it is not a transgressive lag representing sudden marine ingression into the basin. Furthermore, the abundance of
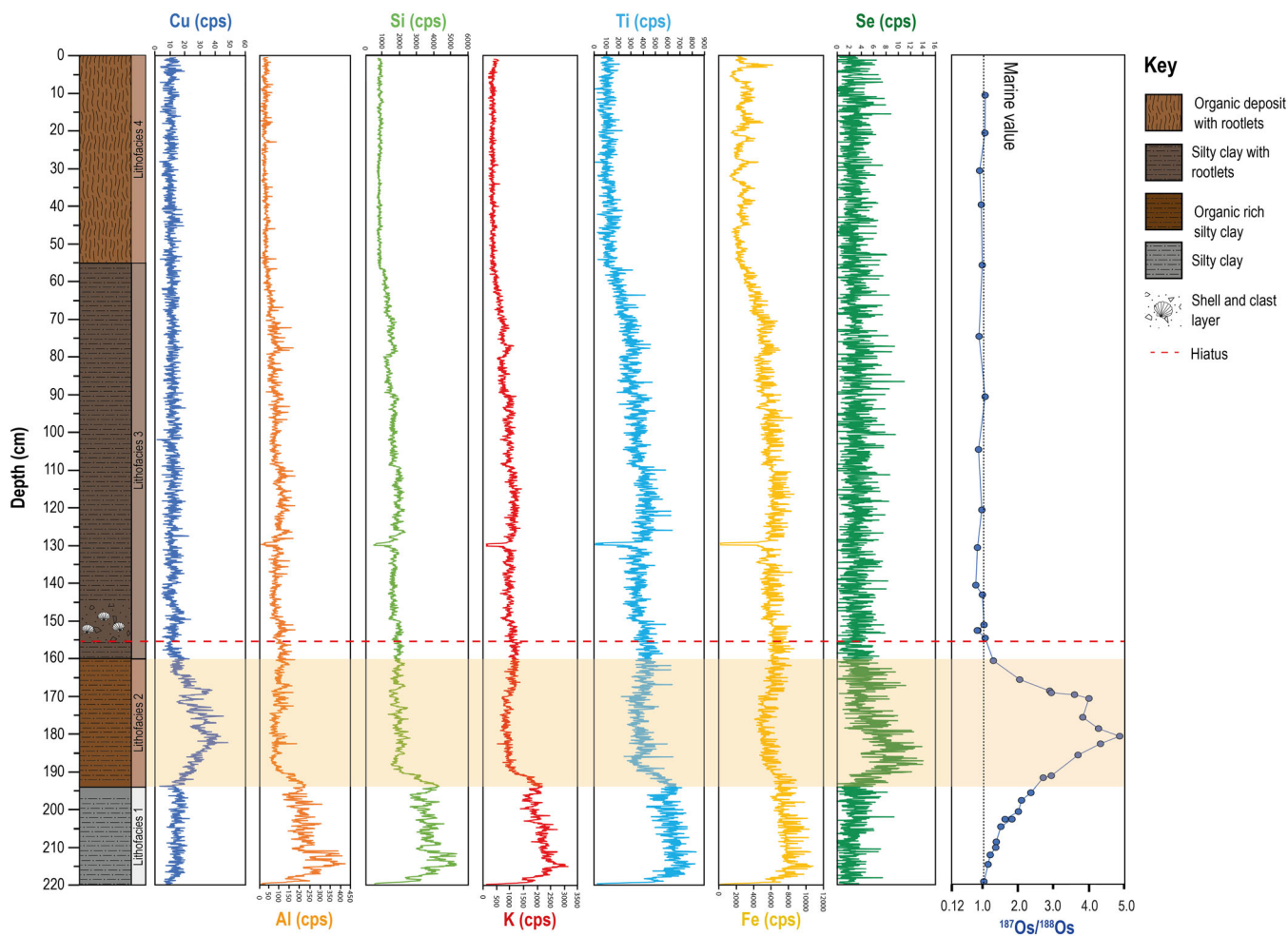
Figure 5. XRF scans for seven elements (Cu, Al, Si, K, Ti, Fe, Se) presented for LDM-20-JT alongside the ^{187}Os/^{188}Os record for correlation. [Color figure can be viewed at wileyonlinelibrary.com]

reworked shells and clasts is not seen throughout the rest of the core, suggesting the observed layer may reflect a single high-energy event. The exact nature of this event is beyond the scope of this study as no regional event is known to be contemporaneous with this hiatus. Yet, based on the sedimentation rate prior to the hiatus, we estimate 30 cm of sediment was removed during the event and the available chronology determined through this study indicates this event occurred between 10 080 and 5500 cal a BP (estimated from the age–depth model; Fig. 6; S2). The Storegga tsunami event, identified elsewhere in Scotland (e.g. Dawson et al., 1988; Long et al., 2016; Bateman et al., 2021) is dated to 8150 ± 30 cal a BP based on radiocarbon dating of tsunami deposits (Bondevik et al., 2012). Based on the chronology of the hiatus presented here any record of the Storegga tsunami event is absent from this site. Following the inferred hiatus, sedimentation rate is modelled to increase to 0.2 mm a^{-1} up until 145 cm before decreasing to 0.08 mm a^{-1} (145–135 cm). Subsequently, an average sedimentation rate of 0.30 mm a^{-1} is estimated between 135 and 55 cm. Following this, L4 records a marked increase in average sedimentation rate to 0.6 mm a^{-1}.

Several new radiocarbon dates improve the chronology of the LDM record considerably from the Hamilton et al. (2015) study and therefore the chronology of the index points are compared to the new age model of this study. Index point 2 yields an age of 14 610–15 240 cal a BP (Hamilton et al., 2015). The stratigraphically equivalent horizon in the LDM-20-JT core is the boundary between L1 and L2, which dates to 14 120 cal a BP. This age is nominally younger but still agrees with the negative tendency of RSL at this time predicted by the glacio-

isostatic models (Bradley et al., 2011; Kuchar et al., 2012). Index point 3 yields an age of 9890–10 180 cal a BP (Hamilton et al., 2015). This correlates to the boundary between L2 and L3 in the LDM-20-JT core, which dates to 10 620 cal a BP; this is not a significant age adjustment and again agrees with the positive tendency of RSL models at this time (Bradley et al., 2011; Kuchar et al., 2012). The final index point, index point 4, yields an age of 310–480 cal a BP (Hamilton et al., 2015). As this index point is based on a diatom transfer function rather than the transition between two lithofacies, we cannot directly relate the age of this index point to the age model of this study, but the RSL models (Bradley et al., 2011; Kuchar et al., 2012) predict gradual RSL fall over this time period so it is unlikely that the improved chronology of this study would result in a significant adjustment in the sea level index point and its tendency.

Discussion

In the following discussion, we consider the full range of proxy evidence for palaeoenvironmental changes recorded in the Loch Duart basin. The aim is to assess the potential applicability of geochemical techniques in palaeoenvironmental and specifically sea-level reconstruction as a way of identifying proxies that could be used in the absence of microfossil data.

Lithofacies 1: Lateglacial marine

Foraminifera are rare through most of L1 (16 820–14 120 cal a BP). However, a small number of *Miliammina fusca*, a brackish-water
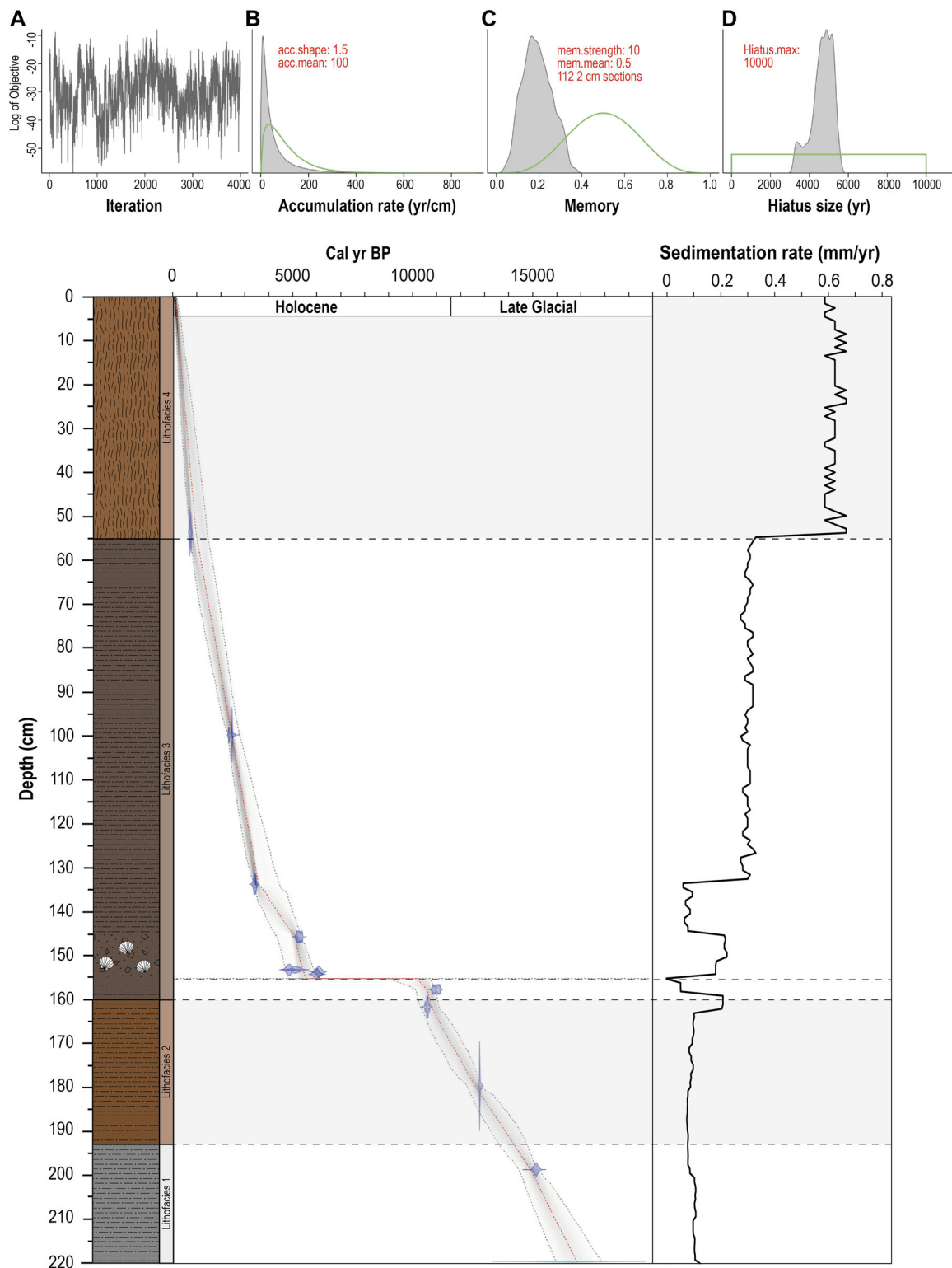
Figure 6. Age–depth model for the LDM-20-JT core using the rbacon (Blaauw & Christen, 2011) package (version 3.1.1) in R. The age–depth model shows calibrated ^{14}C ages depicted in blue with the most accurate age model presented by a red dotted line. The grey stippled lines indicate 95% confidence intervals. Calculated sedimentation rates are depicted on the adjacent plot. Plot (a) depicts iteration history, while plots (b), (c) and (d) show prior, depicted by green lines, and posterior, shown by grey histograms, distributions for accumulation rate (b), memory (c) and hiatus size (d). A sedimentation rate plot is shown to the right. The red dashed line depicts the inferred hiatus and the black dashed lines define the lithofacies. [Color figure can be viewed at wileyonlinelibrary.com]

species often found in association with freshwater-transition conditions (Lloyd & Evans, 2002), are observed. *Miliammina fusca* is notable for its ability to tolerate the lowest salinity and most variable conditions, probably due to its infaunal mode of life (Lloyd & Evans, 2002). This implies that the upper boundary of L1 represents the transition from marine inundation to isolation. Lithofacies 1 correlates with diatom Zone 1 of the nearby

LDM-13-1 core which is dominated by marine diatoms (Hamilton et al., 2015). Utilizing these established biostratigraphic proxies provides the palaeoenvironmental framework on which we can test more novel geochemical proxies.

Low C/N values (4–10) are indicative of algal material (either marine or freshwater), whereas higher C/N values (>20) generally reflect higher-order plant material (typically

terrestrial vegetation; Meyers, 1994). Carbon isotopes ($\delta^{13}C_{org}$) often accompany C/N as a biplot and typical $\delta^{13}C$ and C/N ranges for organic sources have been developed for various coastal environments (Fig. 4) (Lamb et al., 2006). Lithofacies 1 is characterized by relatively high $\delta^{13}C_{org}$ values and low C/N ratios. The majority of these L1 values fall between the range of marine POC, marine DOC and C4 terrestrial plants, which we interpret as the product of a mixed organic carbon pool, but dominated by marine POC and DOC inputs with some smaller contribution by C4 terrestrial plants.

Modern seawater has an osmium isotope ($^{187}Os/^{188}Os$) composition of ~1.04–1.06 reflecting a balance of inputs from radiogenic continental crust and unradiogenic mantle/cosmic dust (e.g. Sharma et al., 1997; Levasseur et al., 1998; Burton et al., 1999; Peucker-Ehrenbrink & Ravizza, 2000; Gannoun & Burton, 2014; Rooney et al., 2016). Submarine volcanism and hydrothermal Os-inputs are characterized as non-radiogenic sources of Os (represented as lower values in $^{187}Os/^{188}Os$ space). The osmium isotopic signature of freshwater systems reflects weathering of the surrounding (radiogenic) continental material, typically producing more radiogenic $^{187}Os/^{188}Os$ water column conditions. The base of L1 yields an osmium signature of 1.059 (118–220 cm); this is a modern marine value which agrees with the diatom-based record of palaeo-salinity (Fig. 7). Upsection, the $^{187}Os/^{188}Os$ values progressively increase (up to 2.379 at 195–196 cm) as gradual isolation of the basin reduces the marine flux, strengthening the impact of the terrestrially derived Os input.

Lithofacies 2: Lateglacial to Early Holocene freshwater

The complete absence of foraminifera in L2 (14 120–10 620 cal a BP) supports the interpretation of a freshwater depositional environment, indicating that the basin had entered a phase of isolation (Fig. 7). The transition between L1 and L2 is characterized by the presence of *Charophyte* oogonia, representing green algae which live submerged in fresh and brackish water (Moore, 1986) and often found at the isolation contact of Scottish isolation basins (e.g. Shennan et al., 2000; Best et al., 2022). The presence of *Charophyte* oogonia thus suggests the transition represents the isolation contact. This interpretation of a reduction in marine influence and associated isolation of the basin is consistent with interpretation based on diatom flora, with oligohalobian-indifferent (freshwater – tolerates low salinity) species such as *Fragilaria construens*, *Epithemia sorex*, *Fragilaria virescens* and *Brachysira brebissonii* dominating the assemblage (Hamilton et al., 2015).

Lithofacies 2 has relatively high C/N ratios and $\delta^{13}C_{org}$ values. The shift to higher C/N ratios in this lithofacies indicates a greater relative input of higher-order plant material (typically terrestrial vegetation rather than aquatic algae) in the organic fraction. The observation that the marine algal contribution was replaced by terrestrial plant organic matter (whether washed into the isolation basin and/or derived from *in situ* growth of freshwater aquatic plants) further supports the interpreted palaeoenvironmental transition to freshwater conditions. The high $\delta^{13}C_{org}$ values of this lithofacies drive $\delta^{13}C$ versus C/N values out of the freshwater field that would be expected based on the biostratigraphic data. Samples from this lithofacies instead cluster towards the C4 terrestrial field. *Myriophyllum alterniflorum*, an aquatic plant, was previously identified at Loch Duart at a depth of 195 cm (Hamilton et al., 2015). *M. alterniflorum* has a median $\delta^{13}C$ signature of −18‰ and an interquartile range of between −22 and −12‰ (Chappuis et al., 2017), providing a possible explanation for both the relatively high observed $\delta^{13}C_{org}$ signature of L2 and

the sample cluster position outside the freshwater DOC, POC and algae fields, in respect to C/N versus $\delta^{13}C$.

The shift in $^{187}Os/^{188}Os$ towards more radiogenic values upsection, eventually culminating in highly radiogenic values
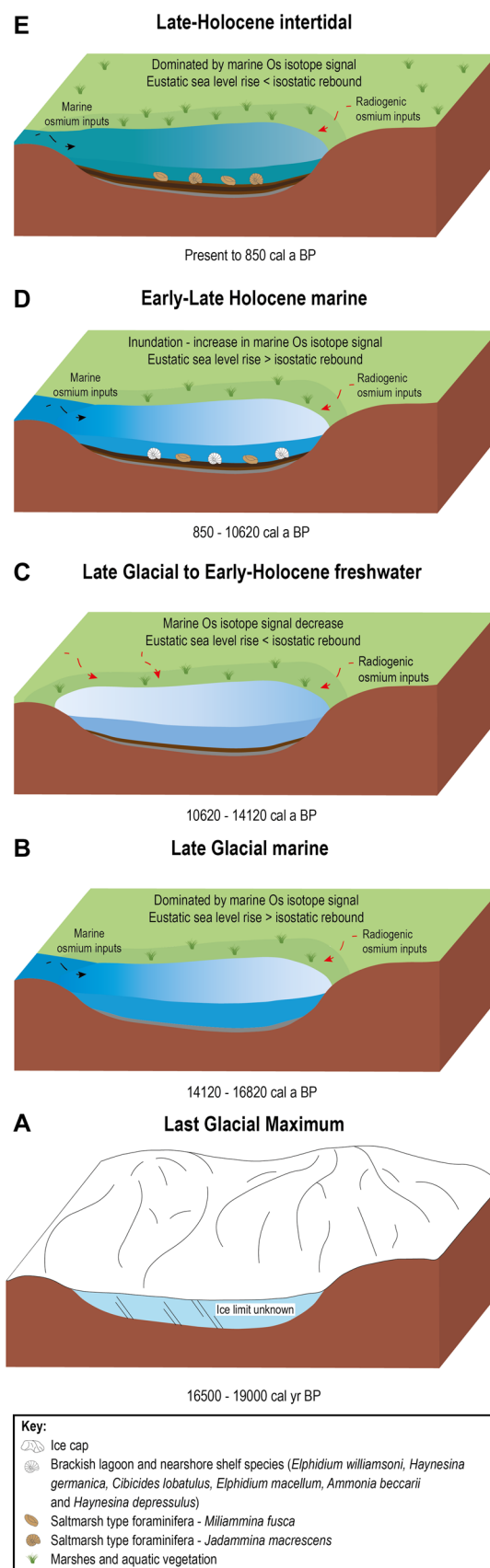

Figure 7. Block diagrams showing the palaeoenvironment evolution of Loch Duart from the Last Glacial Maximum to the present day. See text for discussion. [Color figure can be viewed at wileyonlinelibrary.com]

within L2 (up to 4.89), represents the most notable geochemical feature of this lithofacies. The progressive increase to radiogenic $^{187}Os/^{188}Os$ values indicates a local increase in terrestrially derived osmium sourced from highly radiogenic bedrock. This is coherent with the interpretation of a restricted connection between the basin and the sea and eventual isolation as a result of RSL fall/isostatic rebound, as implied through the microfossil record.

The $^{187}Os/^{188}Os$ signature of L2 is more radiogenic than other restricted marine/non-marine/lacustrine systems such as the Sinemurian Five Card Draw Member (values up to 2.83; Porter et al., 2014), Eocene Green River Formation (1.3–1.5; Cumming et al., 2012) and the Aptian Ipubi Formation black shale (1.8–2.0; Lúcio et al., 2020). However, these values are similar to present-day lake ore deposits of Precambrian shield regions from Sweden, Finland and Russia (3.7–7.8; Peucker-Ehrenbrink & Ravizza, 1996). Therefore, the highly radiogenic L2 $^{187}Os/^{188}Os$ signature is probably a result of continentally derived osmium. In particular, the preferential weathering of felsic minerals, such as biotite, might have contributed to these highly radiogenic values (Peucker-Ehrenbrink & Blum, 1998). Such minerals are present in the Lewisian gneiss – the bedrock material surrounding Loch Duart (Burton et al., 2000). The peak in $^{187}Os/^{188}Os$ values is followed by a decrease approaching the L2–L3 transition, with $^{187}Os/^{188}Os$ reaching near marine values (~1.0) at that boundary. We interpret this trend as gradually returning marine conditions associated with a rise in RSL. The cross-proxy agreement between osmium isotopes, the detailed microfossil record and other established geochemical proxies such as C/N versus $\delta^{13}C$ supports the merit of the osmium isotope system as a tracer of basin isolation and inundation and therefore sea-level fluctuations.

Broad peaks recorded in both selenium (Se) and copper (Cu) at 182 cm, coincident with the peak in $^{187}Os/^{188}Os$ (Fig. 5), further support the interpretation of freshwater conditions during L2 deposition. The c.p.s. of both Cu and Se are above 3 standard deviations and therefore the data are considered a reliable record of the elemental abundance in the lithofacies. The broad peak in Cu-count across L2 is significantly higher than values recorded through the rest of the core. Copper is primarily delivered to sediments in association with OM (organometallic complexes) (Tribovillard et al., 2006) and is released through the decomposition of such complexes. Copper can also coprecipitate with pyrite under reducing conditions, whereby Cu (II) is reduced to Cu (I) (Moore et al., 1988; Huerta-Diaz & Morse, 1990; Tribovillard et al., 2006) and reduced Cu can also form sulphide phases including CuS and CuS_2 (Luther et al., 1980). Therefore, a high Cu abundance might indicate an abundance of OM and an associated strengthening of reducing conditions catalysing Cu-fixation (Tribovillard et al., 2006). Such conditions would be expected in an isolation basin setting and would further support our interpretation of sea level at this time as a restricted basin could trigger salinity stratification and progressive oxygen depletion leading to reducing conditions. Throughout L2 a clear peak in Se is observed, which coincides with the rise in TOC. Selenium enrichment associated with organic matter under anoxic conditions is well known, with Se probably in the form of selenite (SeO_3^{2-}) (Lévesque, 1974; Zhang & Moore, 1997; Tolu et al., 2014; Wen et al., 2014), and this further supports an interpretation of an increase in stratification and anoxia within the basin as a result of RSL fall and basin isolation.

Comparing the $^{187}Os/^{188}Os$, Cu and Se trends with the established palaeoenvironmental record based on biostratigraphy suggests that these geochemical proxies reliably track the nature of the transition between lithofacies during isolation and inundation. The $^{187}Os/^{188}Os$ increase from near fully marine values (1.059) at 118–220 cm to the most radiogenic value (4.89) at 180–181 cm suggests RSL fell between 16 820 and 12 610 cal a BP, thereby suggesting the basin became completely isolated from marine input assuming a constant sedimentation rate and no hiatuses.

The nearby freshwater basin at Oldany provides a maximum 6 m OD elevation for post-Last Glacial Maximum (LGM) sea level in the Assynt region (Hamilton et al., 2015). Combined with raised shoreline evidence (Shennan et al., 2000), this maximum estimate is very close to the model prediction of a maximum post-LGM sea level of ca. 5 m OD (Bradley et al., 2011). A Loch Duart index point constrains RSL to -0.15 ± 0.59 m OD at 199 cm (Hamilton et al., 2015) correlating to the transition between L1 and L2 of this study. By combining the maximum post-LGM sea level of ca. 5 m OD with the index point at Loch Duart and the age model presented here, we can estimate the rate of sea level fall to be 2 mm a^{-1}. If we assume this rate continues upsection, in line with the increasingly more radiogenic $^{187}Os/^{188}Os$ values, sea level would reach -3.03 m OD at 180.5 cm which is the depth that yields the most radiogenic $^{187}Os/^{188}Os$ value of 4.89.

Lithofacies 3: Early–Late Holocene marine

Lagoonal foraminifera species *Elphidium williamsoni* and *Haynesina germanica* appear at 160 cm, implying marine inundation of the basin at the transition between L2 and L3. This is in agreement with the correlated diatom assemblage from core LDM-13-1 (Fig. 2), comprising polyhalobous (marine) species such as *Opephora marina* and *Rhabdonema minutum* with rapidly diminished counts of oligohalobian-indifferent species (Hamilton et al., 2015). Through this transition, C/N ratios decrease from 18.24 (160.5 cm) to 12.12 (152.5 cm) whilst $\delta^{13}C_{org}$ values increase from -22.07 to $-19.90‰$, in line with marine DOC and POC organic carbon sources (Fig. 4), all coherent with the interpretation of a transition to a marine environment. Finally, $^{187}Os/^{188}Os$ values decrease from 1.33 (160–161 cm) to 1.09 (154–155 cm) recording a clear shift towards the present-day seawater signature; this is a strong indication that the Os-isotope system is closely tracking the transition from basin isolation to renewed marine connection.

Based on the most radiogenic $^{187}Os/^{188}Os$ values for L2, between 180–181 and 170–171 cm, complete basin isolation from any tidal influence lasted between 12 610 and 11 550 cal a BP. The progressive lowering of $^{187}Os/^{188}Os$ values (from 4.02 to 1.33) between 170–171 cm (L2) and 160–161 cm (L3) records steady marine inundation between 11 550 and 10 650 cal a BP.

Between 160 and 155 cm the basin is characterized by a lagoonal foraminiferal fauna indicating an intertidal environment from ca. 10.6 to 10.1 ka cal BP. At 155 cm there is a sharp boundary with the overlying shelly, gravel layer (145–155 cm, Fig. 2). This boundary marks an erosive contact and, hence, a hiatus in sedimentation (Fig. 6). Between 145 and 155 cm, the foraminiferal assemblage is characterized by fully marine species (e.g. *Elphidium macellum* and *Cibicides lobatulus*; Figs 2 and 3). The appearance of fully marine fauna could indicate continued RSL rise and a transition from a tidal basin to a subtidal marine embayment by ca. 5500 cal a BP. However, the sudden appearance of large clasts suggests deposition by a high-energy event, which indicates this material may have been sourced from further offshore. This hypothesis provides a reasonable explanation for the absence of fully marine fauna upsection.

Between 140 and 130 cm (4220 and 3320 cal a BP) there is a change in fauna from mixed lagoonal and shallow coastal

fauna to salt marsh type (*Miliammina fusca*). The rapid onset of dominance of *Miliammina fusca* and the accompanied precipitous drop in diversity indicates the transition from near-fully marine conditions toward a basin marked by reduced and highly variable salinity driven by a fall in RSL. We suggest that tidal inundation at high tides supplied some marine water to the basin.

Samples from L3 possess low C/N ratios and high $\delta^{13}C_{org}$ values and largely plot within the marine DOC and marine POC fields (Fig. 4), supporting the general interpretation of a marine depositional setting for L3. A decline in $\delta^{13}C_{org}$ coupled with an increase in C/N ratios at 70 cm towards the top of L3 indicates an increase in freshwater aquatic and terrestrial organic matter input relative to marine organic matter. The uppermost L3 sample lies just below the marine DOC field, indicating a decreasing marine influence upsection.

The upper L3 osmium isotopic signature records very little variability; $^{187}Os/^{188}Os$ values remain consistently close to the osmium signature of modern marine water implying persistent marine inundation. Whilst this record agrees with the overall body of proxies suggesting a return to marine conditions near the base of L3, it appears that the osmium data presented here are less sensitive to the subtle shift in marine influence through L3 due to continued tidal influence introducing a marine osmium-isotope composition into the basin and limited input of terrestrially transported material.

Lithofacies 4: Late Holocene intertidal

The transition to L4 (850 cal a BP to present) is characterized by a reduction in *Miliammina fusca* and the appearance and dominance of *Jadammina macrescens*. This shift in faunal assemblage is probably associated with continued RSL fall and reduced marine influence as tidal inundation is reduced, perhaps limited to high tides. At the present day the basin is virtually fully infilled and characterized by fringing salt marsh vegetation inundated only at high tides. *Jadammina macrescens* tends to dominate high salt marsh environments and is also found in modern tidal lagoons near the limit of marine inundation (e.g. Horton et al., 1999; Lloyd & Evans, 2002). Therefore, we interpret the presence and dominance of *J. macrescens* as evidence of a lagoonal depositional setting becoming increasingly isolated from marine inundation (Lloyd & Evans, 2002). Today, Loch Duart is actively transitioning from a lagoon to a salt marsh (Fig. 7). These results are consistent with an observed reduction in polyhalobous species coupled with an increase in oligohalobian-indifferent and mesohalobous (brackish) species (Hamilton et al., 2015). The L3–L4 boundary marks a trend towards increasing C/N ratios and decreasing $\delta^{13}C_{org}$ values. The samples from L4 cluster within and just above the freshwater DOC and C3 terrestrial plant fields, which we associate with a decrease in the input of marine organic matter relative to freshwater carbon inputs.

The osmium isotopic signature of this lithofacies remains near present-day seawater values, implying that the basin is not completely isolated from marine input. While the microfossil records illustrate a reduction in marine influence within the basin, we believe that the continued osmium isotope marine signature of L4 is due to the continued tidal influence in the basin with limited input of terrestrially transported material. This, to a certain extent, may be due to the setting of Loch Duart with no significant stream input at the present day (Fig. 1). As discussed, the microfossil records show an increase in salt marsh-type species with the foraminifera record showing an increase in *Jadammina macrescens* and *Miliammina fusca*, and the diatom record showing an increase in oligohalobian-indifferent and mesohalobous (brackish)

species. It is important to consider their respective salinity tolerances here. Polyhalobous species thrive in fully marine conditions, with a salinity exceeding 30 practical salinity units (p.s.u.), mesohalobous diatoms thrive in salt concentrations of between 0.2 and 30 p.s.u. and oligohalobian-indifferent diatoms generally occur in salt concentrations less than 0.2 p.s.u. (Hustedt, 1953). Whilst oligohalobian-indifferent and mesohalobous (brackish) species are most dominant throughout L4, polyhalobous species are also present and constitute <20% of the total count, which suggests that salinity was highly variable over this time as all three species groups favouring salinities ranging from <0.2 to >30 p.s.u. could survive. Today the basin is inundated at high tide and the surrounding ground becomes entirely saturated with seawater. Limited freshwater drainage into the basin, due to the lack of an inflowing stream, limits the amount of terrestrially derived material to influence the osmium isotopic signature. This probably explains why the osmium isotope signature remains at or close to the present-day marine signature as the basin has remained connected to the open sea during the tidal cycle meaning a continued influx of a marine osmium isotopic signature.

Implications of the $^{187}Os/^{188}Os$ and $^{187}Re/^{188}Os$ records

Here, the $^{187}Os/^{188}Os$ isotope system has been applied to an isolation basin and has been successfully shown to be a powerful tracer of basin isolation and inundation. Lithofacies 1 records a marine isotopic signature of 1.059 at its base reflecting the connection between the basin and the open sea (Fig. 8a). Upsection L1 records more radiogenic $^{187}Os/^{188}Os$ values increasing up to 2.38. This reflects an increase in terrestrially derived osmium and a decrease in marine osmium isotope influence due to RSL fall. This trend continues into L2 with a further increase towards more radiogenic $^{187}Os/^{188}Os$ values recorded (up to 4.89). This is due to a further reduction in marine influence and a relative increase in continentally derived radiogenic osmium inputs as the basin becomes isolated from the sea. This shift reflects the preferential weathering of felsic minerals, such as biotite, which are known to be present in the Lewisian gneiss bedrock surrounding the field site (Burton et al., 2000). The markedly radiogenic values of L2 imply the basin did not experience marine connection and entered a phase of isolation (Fig. 8b). Upsection in L2 $^{187}Os/^{188}Os$ values show a gradual decrease to less radiogenic values, and this trend continues into L3, where modern marine values are attained once more. This implies RSL rise allowing renewed marine connection, the end of isolation and the re-introduction of a marine osmium-isotope composition into the basin (Fig. 8c). The osmium isotopic signature through L3 and L4 remains relatively constant throughout with values ranging from 0.83 to 1.09. These values are near those of present-day seawater implying the basin did not reach full isolation again but rather the basin has experienced continued tidal inundation (Fig. 8d).

This history of basin isolation bracketed by phases of marine connection is clearly recorded in the $^{187}Os/^{188}Os$ record, with marine periods recording a modern marine signature and the freshwater phase possessing a markedly more radiogenic signature. The proxy is less sensitive to the subtle fluctuations between more brackish and more marine conditions through L3 and L4. We believe this is due to a continued, albeit reduced, marine influence as a result of tidal influence throughout L3 and L4 introducing a marine osmium-isotope composition into the basin coupled with the low freshwater drainage due to lack of riverine input to the basin at the present day. This record highlights the usefulness of this novel method,
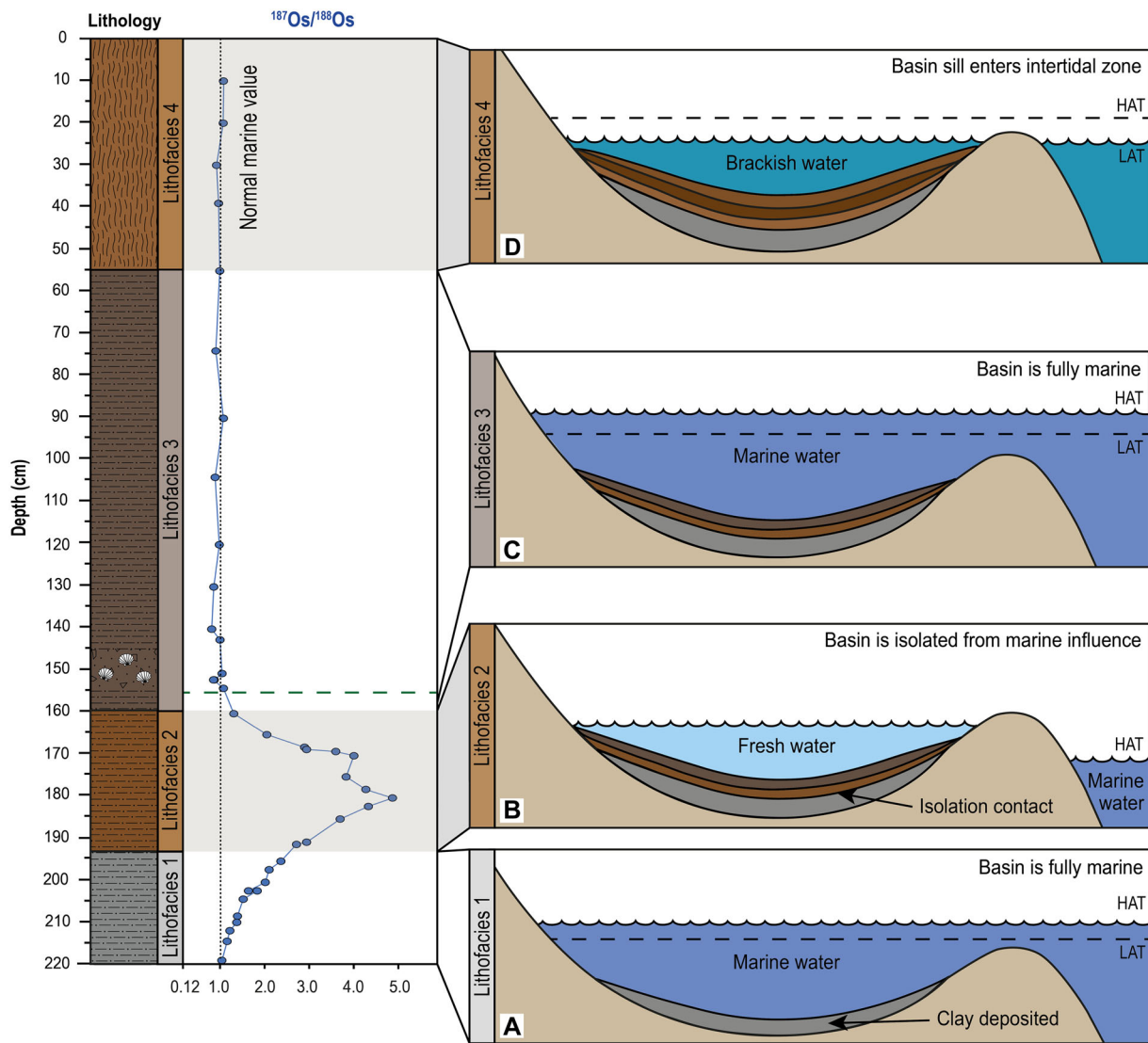
Figure 8. The $^{187}Os/^{188}Os$ record of LDM-20-JT with schematic diagrams illustrating the depositional environment of each lithofacies and the isolation process, modified from Long et al. (2011). LAT, lowest astronomical tide level; HAT, highest astronomical tide level. [Color figure can be viewed at wileyonlinelibrary.com]

which is not reliant on microfossil preservation, as a tracer of basin isolation and inundation and, therefore, RSL.

Organic matter diversity in sedimentary rocks is considered to play a key role in Re–Os uptake/fractionation and thus yielding variable $^{187}Re/^{188}Os$ ratios (Harris et al., 2013; Liu et al., 2020; Pietras et al., 2022). In contrast, homogenous organic matter content may lead to similar $^{187}Re/^{188}Os$ ratios by providing uniform chelating sites for both Re and Os (Pietras et al., 2022). Whilst here we have no direct evidence of the diversity of organic matter types present throughout our Loch Duart record, each lithofacies records a distinct environment with associated changes in $\delta^{13}C_{org}$ and C/N which may relate to varied organic matter types.

There is little variation in $^{187}Re/^{188}Os$ ratios across L1 possibly due to the low TOC content of the sediment as it is a silty clay. Lithofacies 2 shows some small variation with two peaks coincident with the peaks in the $^{187}Os/^{188}Os$ record; the interpreted restricted nature of the basin during the deposition of L2 could explain the low variation in $^{187}Re/^{188}Os$ ratios as previous work on deposition in a restricted basin and with a hence lower diversity of organic matter yielded a narrow range of $^{187}Re/^{188}Os$ ratios (Pietras et al., 2022). Lithofacies 3 records much higher and more varied $^{187}Re/^{188}Os$ ratios and is interpreted to have been deposited during a period of renewed

marine connection probably allowing a greater diversity of organic matter types. Across the transition between L3 and L4, there is a dramatic decrease in $^{187}Re/^{188}Os$ values. Across the same transition the $\delta^{13}C_{org}$ and C/N values also shift suggesting as discussed a change from a marine to a tidally inundated basin. This shift would again probably reduce the organic matter diversity which could explain the abrupt decrease in $^{187}Re/^{188}Os$ ratios across the boundary. This record implies that with further study of the relationship between $^{187}Re/^{188}Os$ ratios and organic matter type, Re and Os systematics beyond $^{187}Os/^{188}Os$ could be used to imply environmental change.

Conclusions

- The foraminiferal data presented here agree with the biostratigraphic interpretations based on diatoms from Hamilton et al. (2015). This biostratigraphic compilation provides a suitable framework for testing more novel proxies. Variations in $\delta^{13}C_{org}$ and C/N broadly follow the foraminifera- and diatom-based record of palaeosalinity with periods of marine connection characterized by low C/N ratios (9–13) and relatively ^{13}C-enriched $\delta^{13}C_{org}$ values (−24 to −15‰), in contrast with more ^{13}C-depleted $\delta^{13}C_{org}$ values (−26 to

−25‰) recorded in intertidal sediments. Therefore, this study further demonstrates that changes in the source of organic material, which possess unique $\delta^{13}C_{org}$ and C/N signatures, can be used to track marine inundation and basin isolation.

- The XRF analysis also yields new insight into the freshwater lithofacies (L2) with peaks in both copper and selenium. Both are suggestive of a period of anoxia during the deposition of L2, interpreted to reflect stratification within the basin as a result of RSL fall (isostatic rebound) and basin isolation.

- Application of the osmium isotope system shows that periods of connection between the basin and the sea are associated with $^{187}Os/^{188}Os$ values similar to those of modern seawater (~1.04–1.06). Conversely, periods of isolation from the open ocean are characterized by distinctly more radiogenic $^{187}Os/^{188}Os$ values (up to 4.89) reflecting a decreased marine influence. These trends are in remarkable agreement with the biostratigraphic reconstructions. The $^{187}Os/^{188}Os$ data and the age model presented here combined with existing sea level limiting points yield a rate of sea level fall of 2 mm a^{-1} between 16.8 and 14.1 ka cal BP. This novel application of the osmium isotope system demonstrates another merit of the isotope tracer in that it not only distinguishes marine and freshwater environments but can also track the evolution of seawater influence into the basin over time when combined with a high-precision age model.

- The close multiproxy agreement in RSL reconstruction from both $^{187}Os/^{188}Os$ data and traditional biostratigraphic methods indicates that the $^{187}Os/^{188}Os$ isotope system can be an effective tracer of RSL within isolation basins. Periods of marine regression, basin isolation and freshwater deposition preserve perturbations towards more radiogenic values, whereas periods of marine deposition associated with the connection of the basin to the open ocean record values consistent with the present-day normal marine osmium isotopic signature. Although the system can be less sensitive to brackish phases in nearshore settings, its ability to distinguish freshwater from marine periods of deposition demonstrates the effectiveness of osmium as a tracer of relative sea level and its potential use at sites with poor preservation of microfossils.

Data availability statement

The data that supports the findings of this study are available in the supplementary material of this article. The authors confirm that the data supporting the findings of this study are available within the article and its supplementary materials.

Supporting information

Additional supporting information can be found in the online version of this article.

Abbreviations. BIIS, British and Irish Ice Sheet; DOC, dissolved organic carbon; HAT, highest astronomical tide; LAT, lowest astronomical tide; LGM, Last Glacial Maximum; MHWST, mean high water spring tide; POC, particulate organic carbon; RSL, relative sea level; TOC, total organic carbon; XRF, X-ray fluorescence.

References

Andrews, J.E., Samways, G., Dennis, P.F. & Maher, B.A. (2000) Origin, abundance and storage of organic carbon and sulphur in the Holocene Humber Estuary: emphasizing human impact on storage changes. *Geological Society, London, Special Publications*, 166(1), 145–170.

Arthur, M.A., Dean, W.E. & Claypool, G.E. (1985) Anomalous ^{13}C enrichment in modern marine organic carbon. *Nature*, 315, 216–218.

Bateman, M.D., Kinnaird, T.C., Hill, J., Ashurst, R.A., Mohan, J., Bateman, R.B.I. et al. (2021) Detailing the impact of the Storegga Tsunami at Montrose, Scotland. *Boreas*, 50(4), 1059–1078.

Best, L., Simms, A.R., Brader, M., Lloyd, J., Sefton, J. & Shennan, I. (2022) Local and regional constraints on relative sea-level changes in southern Isle of Skye, Scotland, since the Last Glacial Maximum. *Journal of Quaternary Science*, 37(1), 59–70.

Blaauw, M. & Christen, J.A. (2011) Flexible paleoclimate age–depth models using an autoregressive gamma process. *Bayesian Analysis*, 6(3), 457–474.

Bondevik, S., Stormo, S.K. & Skjerdal, G. (2012) Green mosses date the Storegga tsunami to the chilliest decades of the 8.2 ka cold event. *Quaternary Science Reviews*, 45, 1–6.

Bradley, S.L., Milne, G.A., Shennan, I. & Edwards, R. (2011) An improved glacial isostatic adjustment model for the British Isles. *Journal of Quaternary Science*, 26(5), 541–552.

Bronk Ramsey, C. (2009) Bayesian analysis of radiocarbon dates. *Radiocarbon*, 51(1), 337–360.

Burton, K.W., Bourdon, B., Birck, J.L., Allègre, C.J. & Hein, J.R. (1999) Osmium isotope variations in the oceans recorded by Fe-Mn crusts. *Earth and Planetary Science Letters*, 171(1), 185–197.

Burton, K.W., Capmas, F., Birck, J.L., Allègre, C.J. & Cohen, A.S. (2000) Resolving crystallisation ages of Archean mafic-ultramafic rocks using the Re-Os isotope system. *Earth and Planetary Science Letters*, 179(3–4), 453–467.

Chappuis, E., Seriñá, V., Martí, E., Ballesteros, E., & Gacia, E. (2017). 'Decrypting stable-isotope (δ13C and δ15N) variability in aquatic plants'. *Freshwater Biology* 62(11): 1807–1818.

Cohen, A.S., Coe, A.L., Bartlett, J.M. & Hawkesworth, C.J. (1999) Precise Re-Os ages of organic-rich mudrocks and the Os isotope composition of Jurassic seawater. *Earth and Planetary Science Letters*, 167(3-4), 159–173.

Cumming, V.M., Selby, D. & Lillis, P.G. (2012) 'Re-Os geochronology of the lacustrine Green River Formation: Insights into direct depositional dating of lacustrine successions, Re-Os systematics and paleocontinental weathering'. *Earth and Planetary Science Letters*, 359–360, 194–205.

Dawson, A.G., Long, D. & Smith, D.E. (1988) The Storegga Slides: Evidence from Eastern Scotland for a possible tsunami. *Marine Geology*, 82, 271–276.

Ehrenbrink, B.P. & Ravizza, G. (1996) Continental runoff of osmium into the Baltic Sea. *Geology*, 24(4), 327–330.

Flemming, N.C. (1982) Multiple regression analysis of earth movements and eustatic sea-level change in the United Kingdom in the past 9000 years. *Proceedings of the Geologists' Association*, 93(1), 113–125.

Gannoun, A. & Burton, K.W. (2014) High precision osmium elemental and isotope measurements of North Atlantic seawater. *Journal of Analytical Atomic Spectrometry*, 29(12), 2330–2342.

Hamilton, C.A., Lloyd, J.M., Barlow, N.L.M., Innes, J.B., Flecker, R., & Thomas, C.P. (2015). Late Glacial to Holocene relative sea-level change in Assynt, northwest Scotland, UK. *Quaternary Research (United States)* 84(2): 214–222.

Harkness, D.D. (1983) The extent of natural ^{14}C deficiency in the coastal environment of the United Kingdom. *PACT, Journal of the European Study Group on Physical, Chemical and Mathematical Techniques Applied to Archaeology*, 8(IV.9), 351–364.

Harris, N.B., Mnich, C.A., Selby, D. & Korn, D. (2013) Minor and trace element and re-os chemistry of the upper devonian woodford shale, permian basin, west texas: Insights into metal abundance and basin processes. *Chemical Geology*, 356, 76–93.

Heaton, T.J., Köhler, P., Butzin, M., Bard, E., Reimer, R.W., Austin, W.E.N. et al. (2020) Marine20 - The Marine Radiocarbon Age Calibration Curve (0-55,000 cal BP). *Radiocarbon*, 62(4), 779–820.

Horton, B.P., Edwards, R.J. & Lloyd, J.M. (1999) UK intertidal foraminiferal distributions: implications for sea-level studies. *Marine Micropaleontology*, 36, 205–223.

Huerta-Diaz, M.A. & Morse, J.W. (1990) A Quantitative Method for Determination of Trace Metal Concentrations in Sedimentary Pyrite. *Marine Chemistry*, 29, 119–144.

Hustedt, F. (1953) Die Systematik der Diatomeen in ihren Beziehungen zur Geologie und Okologie nebst einer Revision des Halobiensystems. *Svensk Botanisk Tidskrift*, 47, 509–519.

Johnstone, G. & Mykura, W. (1989) British Regional Geology: The Northern Highlands of Scotland 4th ed, 4th edn. Nottingham: British Geological Survey *British regional geology: the Northern Highlands of Scotland*.

Krabbendam, M. & Bradwell, T. (2014) Quaternary evolution of glaciated gneiss terrains: Pre-glacial weathering vs. glacial erosion. *Quaternary Science Reviews*, 95, 20–42.

Kuchar, J., Milne, G., Hubbard, A., Patton, H., Bradley, S., Shennan, I. et al. (2012) Evaluation of a numerical model of the British-Irish ice sheet using relative sea-level data: Implications for the interpretation of trimline observations. *Journal of Quaternary Science*, 27(6), 597–605.

Kuroda, J., Jiménez-Espejo, F.J., Nozaki, T., Gennari, R., Lugli, S., Manzi, V. et al. (2016) Miocene to Pleistocene osmium isotopic records of the Mediterranean sediments. *Paleoceanography*, 31(1), 148–166.

Lamb, A.L., Wilson, G.P. & Leng, M.J. (2006) A review of coastal palaeoclimate and relative sea-level reconstructions using δ13C and C/N ratios in organic material. *Earth-Science Reviews*, 75(1–4), 29–57.

Levasseur, S., Birck, J.-L. & Allègre, C.J. (1999) The osmium riverine flux and the oceanic mass balance of osmium. *Earth and Planetary Science Letters*, 174, 7–23.

Levasseur, S., Birck, J.-L. & Allègre, C.J. (1998) Direct Measurement of Femtomoles of Osmium and the $^{187}Os/^{186}Os$ Ratio in Seawater. *Science*, 282(5387), 272–274.

Lévesque, M. (1974) Selenium distribution in Canadian soil profiles. *Canadian Journal of Soil Science*, 54(1), 63–68.

Liu, Z., Selby, D., Hackley, P.C. & Jeffrey Over, D. (2020) Evidence of wildfires and elevated atmospheric oxygen at the Frasnian-Famennian boundary in New York (USA): Implications for the Late Devonian mass extinction. *Bulletin of the Geological Society of America*, 132(9–10), 2043–2054.

Lloyd, J. (2000) Combined foraminiferal and thecamoebian environmental reconstruction from an isolation basin in NW Scotland: Implications for sea-level studies. *Journal of Foraminiferal Research*, 30(4), 294–305.

Lloyd, J.M. & Evans, J.R. (2002) Contemporary and fossil foraminifera from isolation basins in northwest Scotland. *Journal of Quaternary Science*, 17(5–6), 431–443.

Lo Giudice Cappelli, E. & Austin, W.E.N. (2020) Marine Bivalve Feeding Strategies and Radiocarbon Ages in Northeast Atlantic Coastal Waters. *Radiocarbon*, 62(1), 107–125.

Long, A.J., Barlow, N.L.M., Dawson, S., Hill, J., Innes, J.B., Kelham, C. et al. (2016) Lateglacial and Holocene relative sea-level changes and first evidence for the Storegga tsunami in Sutherland, Scotland. *Journal of Quaternary Science*, 31(3), 239–255.

Long, A.J., Woodroffe, S.A., Roberts, D.H. & Dawson, S. (2011) Isolation basins, sea-level changes and the Holocene history of the Greenland Ice Sheet. *Quaternary Science Reviews*, 30(27–28), 3748–3768.

Lu, X., Kendall, B., Stein, H.J. & Hannah, J.L. (2017) Temporal record of osmium concentrations and $^{187}Os/^{188}Os$ in organic-rich mudrocks: Implications for the osmium geochemical cycle and the use of osmium as a paleoceanographic tracer. *Geochimica et Cosmochimica Acta*, 216, 221–241.

Lúcio, T., Souza Neto, J.A. & Selby, D. (2020) 'Late Barremian/Early Aptian Re–Os age of the Ipubi Formation black shales: Stratigraphic and paleoenvironmental implications for Araripe Basin, northeastern Brazil'. *Journal of South American Earth Sciences*, 102, 102699.

Luther, G.W., Meyerson, A.L., Krajewski, J., & Hires, R.I. (1980). Metal sulfides in estuarine sediments. *Journal of Sedimentary Petrology* 50(4), 1117–1120.

Mackie, E.A.V., Leng, M.J., Lloyd, J.M. & Arrowsmith, C. (2005) Bulk organic δ13C and C/N ratios as palaeosalinity indicators within a Scottish isolation basin. *Journal of Quaternary Science*, 20(4), 303–312.

Meyers, P.A. (1994) 'Preservation of elemental and isotopic source identification of sedimentary organic matter'. *Chemical Geology*, 114(3-4), 289–302.

Moore, J.A. (1986) *Charophytes of Great Britain and Ireland*. Botanical Society of the British Isles.

Moore, J.N., Ficklin, W.H. & Johns, C. (1988) 'Partitioning of Arsenic and Metals in Reducing Sulfidic Sediments'. *Environmental Science & Technology*, 22(4), 432–437.

Müller, A. & Mathesius, U. (1999) 'The palaeoenvironments of coastal lagoons in the southern Baltic Sea, I. The application of sedimentary C org =N ratios as source indicators of organic matter'. *Palaeogeography, Palaeoclimatology, Palaeoecology*, 145(1–3), 1–16.

Murray, J. (1971) *An Atlas of British Recent Foraminiferids*. London: Heinemann Educational Books. p. 244

Murray, J. (1979) British nearshore Foraminiferids. In: Kermack, D.M. & Barnes, R.S.K., (eds) *Synopsis of the British fauna (New Series) 16*. London: Academic Press. p. 68 In:.

Ownsworth, E., Selby, D., Lloyd, J., Knutz, P., Szidat, S., Andrews, J. et al. (2023) Tracking sediment delivery to central Baffin Bay during the past 40 kyrs: Insights from a multiproxy approach and new age model. *Quaternary Science Reviews*, 308, 108082. Available at https://doi.org/10.1016/j.quascirev.2023.108082

Paquay, F.S. & Ravizza, G. (2012) Heterogeneous seawater $^{187}Os/^{188}Os$ during the Late Pleistocene glaciations. *Earth and Planetary Science Letters*, 349–350, 126–138.

Peucker-Ehrenbrink, B. (2002) Comment on "residence time of osmium in the oceans" by Rachel Oxburgh. In *Geochemistry, Geophysics, Geosystems*, 3(10), 1–4.

Peucker-Ehrenbrink, B. & Blum, J.D. (1998) Re-Os isotope systematics and weathering of Precambrian crustal rocks: Implications for the marine osmium isotope record. *Geochimica et Cosmochimica Acta*, 62(19), 3193–3203.

Peucker-Ehrenbrink, B. & Jahn, B. (2001) Rhenium-osmium isotope systematics and platinum group element concentrations: Loess and the upper continental crust. *Geochemistry, Geophysics, Geosystems*, 2(10), n/a.

Peucker-Ehrenbrink, B. & Ravizza, G. (2000) The marine osmium isotope record. *Terra Nova*, 12(5), 205–219.

Pietras, J.T., Dennett, A., Selby, D. & Birdwell, J.E. (2022) The role of organic matter diversity on the Re-Os systematics of organic-rich sedimentary units: Insights into the controls of isochron age determinations from the lacustrine Green River Formation. *Chemical Geology*, 604, 120939.

Porter, S.J., Smith, P.L., Caruthers, A.H., Hou, P., Gröcke, D.R. & Selby, D. (2014) New high resolution geochemistry of Lower Jurassic marine sections in western North America: A global positive carbon isotope excursion in the Sinemurian? *Earth and Planetary Science Letters*, 397, 19–31.

Ravizza, G. & Turekian, K.K. (1989) 'Application of the 187Re-187Os system to black shale geochronometry'. *Geochimica et Cosmochimica Acta*, 53(12), 3257–3262.

Reimer, P.J., Austin, W.E.N., Bard, E., Bayliss, A., Blackwell, P.G., Bronk Ramsey, C. et al. (2020) The IntCal20 Northern Hemisphere Radiocarbon Age Calibration Curve (0-55 cal kBP). *Radiocarbon*, 62(4), 725–757.

Reimer, P.J., Bard, E., Bayliss, A., Beck, J.W., Blackwell, P.G., Ramsey, C.B. et al. (2013) 'IntCal13 and Marine13 Radiocarbon Age Calibration Curves 0–50,000 Years cal BP'. *Radiocarbon*, 55(4), 1869–1887.

Reimer, P.J. & Reimer, R.W. (2001) A marine reservoir correction database and on-line interface. *Radiocarbon*, 43(2A), 461–463.

Reisberg, L. & Lorand, J.P. (1995) Longevity of sub-continental mantle lithosphere from osmium isotope systematics in orogenic peridotite massifs. *Nature*, 376, 159–162.

Rooney, A.D., Selby, D., Lloyd, J.M., Roberts, D.H., Lückge, A., Sageman, B.B. et al. (2016) 'Tracking millennial-scale Holocene glacial advance and retreat using osmium isotopes: Insights from the Greenland ice sheet'. *Quaternary Science Reviews*, 138, 49–61.

Schimmelmann, A., Albertino, A., Sauer, P.E., Qi, H., Molinie, R. & Mesnard, F. (2009) 'Nicotine, acetanilide and urea multi-level2H-,13C- and15N-abundance reference materials for continuous-flow isotope ratio mass spectrometry'. *Rapid Communications in Mass Spectrometry*, 23(22), 3513–3521.

Selby, D. & Creaser, R.A. (2003) 'Re-Os geochronology of organic rich sediments: An evaluation of organic matter analysis methods'. *Chemical Geology*, 200(3–4), 225–240.

Sharma, M., Papanastassiou, D.A. & Wasserburg, G.J. (1997) The concentration and isotopic composition of osmium in the oceans. *Geochimica et Cosmochimica Acta*, 61(16), 3287–3299.

Shennan, I., Bradley, S. et al. (2006a) 'Relative sea-level changes, glacial isostatic modelling and ice-sheet reconstructions from the British Isles since the Last Glacial Maximum'. *Journal of Quaternary Science*, 21(6), 585–599.

Shennan, I., Hamilton, S., Hillier, C., Hunter, A., Woodall, R., Bradley, S., et al. (2006b). 'Relative sea-level observations in western Scotland since the Last Glacial Maximum for testing models of glacial isostatic land movements and ice-sheet reconstructions'. *Journal of Quaternary Science* 21(6), 601–613.

Shennan, I., Hamilton, S., Hillier, C. & Woodroffe, S. (2005) 'A 16 000-year record of near-field relative sea-level changes, northwest Scotland, United Kingdom'. *Quaternary International*, 133–134(1 SUPPL), 95–106.

Shennan, I., Lambeck, K., Horton, B., Innes, J., Lloyd, J., McArthur, J. et al. (2000) 'Late Devensian and Holocene records of relative sea-level changes in northwest Scotland and their implications for glacio-hydro-isostatic modelling'. *Quaternary Science Reviews*, 19(11), 1103–1135.

Smith, D.E., Barlow, N.L.M., Bradley, S.L., Firth, C.R., Hall, A.M., Jordan, J.T. et al. (2019) 'Quaternary sea level change in Scotland'. *Earth and Environmental Science Transactions of the Royal Society of Edinburgh*, 110(1–2), 219–256.

Szidat, S., Salazar, G.A., Vogel, E., Battaglia, M., Wacker, L., Synal, H.A. et al. (2014) 14 C Analysis and Sample Preparation at the New Bern Laboratory for the Analysis of Radiocarbon with AMS (LARA). *Radiocarbon*, 56(2), 561–566.

Tolu, J., Thiry, Y., Bueno, M., Jolivet, C., Potin-Gautier, M. & Le Hécho, I. (2014) 'Distribution and speciation of ambient selenium in contrasted soils, from mineral to organic rich'. *Science of the Total Environment*, 479–480(1), 93–101.

Tribovillard, N., Algeo, T.J., Lyons, T. & Riboulleau, A. (2006) 'Trace metals as paleoredox and paleoproductivity proxies: An update'. *Chemical Geology*, 232(1–2), 12–32.

Troels-Smith, J. (1955) Characterization of unconsolidated sediments. 3rd edn. *Geological Survey of Denmark IV*, 3, 1–73.

Walker, R.J., Carlson, R.W., Shirey, S.B. & Boyd, F. R. (1989) Os, Sr, Nd, and Pb isotope systematics of southern African peridotite xenoliths: Implications for the chemical evolution of subcontinental mantle. *Geochimica et Cosmochimica Acta*, 53, 1583–1595.

Wen, H., Carignan, J., Chu, X., Fan, H., Cloquet, C., Huang, J. et al. (2014) 'Selenium isotopes trace anoxic and ferruginous seawater conditions in the Early Cambrian'. *Chemical Geology*, 390, 164–172.

Zhang, Y. & Moore, J.N. (1997) Interaction of selenate with a wetland sediment. *Applied Geochemistry*, 12(5), 685–691.